Electron-Phonon Scattering Rates in GaAs/AlGaAs 2DEGs Below 0.5K

A Dissertation

Presented to the Faculty of the Graduate School

of

Yale University

in candidacy for the degree of

Doctor of Philosphy

by

Anurag Mittal

December 1996

Abstract

Electron-Phonon Scattering Rates in GaAs/AlGaAs 2DEGs below 0.5K

Anurag Mittal

Yale University

1996

This study is an experimental investigation of heat flow in a GaAs 2DEG below 0.5K. The heat flow due to phonon emission shows a temperature dependence proportional to fifth power of the electron temperature. The measurements for the cleanest sample constitute the first experimental verification of the theoretical predictions in the clean limit for the screened Bloch-Grüneisen regime [Price, 1982].

The electron-phonon scattering rates, extracted from these heat flow measurements, show a temperature dependence proportional to the third power of the electron temperature. The electron-phonon scattering rate is found to increase with decreasing mean free path over nearly one decade of variation in mean free path. These are the first measurements of the electron-phonon scattering rate as a function of the mean free path in a GaAs/AlGaAs 2DEG.

Acknowledgments

My thesis bears a mark of all those who have contributed to my scientific growth. But what is not reflected here in black and white are the contributions by many to my personal growth, without which this achievement would not have been possible. Thank you all.

I am thankful to my advisor, Prof. Daniel E. Prober for allowing me to branch off from the existing project and coin my own research topic quite late along the graduate school ladder, and for having the confidence in my abilities to do independent research. His ability to extract the gist out of a seemingly complicated scientific idea is both rare and inspirational. He has taught me the importance of a good presentation, and the skills necessary to carry it out.

Prof. Bob Wheeler has been a source of constant inspiration ever since I got to know him. His office door was always open for me to come in, throw out whatever came to my mind and be shouted back. In him I found the perfect plane for reflection of "sound" scientific ideas. His uncompromising attitude for accurate measurements and physics fundamentals provided a strong foundation to my work. In him, I also found somebody who if needed was willing to get his hands dirty with the nuts and bolts.

Prof. Richard Chang and Prof. Peter Kindlmann provided valuable insights into post-graduate school life. I am grateful to Prof. Steve Girvin at Indiana University for taking the time out to respond promptly to my email queries during my last couple of weeks at Yale and to Dr. Bob Sacks at Ohio State University for growing the wafers for the experimental work. I thank the members of my thesis committee, Prof. Richard Chang, Prof. Karin Rabe, Prof. Bob Wheeler and Prof. Dan Prober, and the external reader Prof. Michael Reyzer, for their time and patience in examining this work. I would especially like to thank my friend Stephan for honing my verbose script with his immaculate German grammar.

I was introduced to the traditions of Prober lab by Oded Millo and Mark Keller. In their company, I learnt many valuable experimental skills. Others with whom I have overlapped include Mike Gadis, Jim McCambridge, Stephan Friedrich, Nick Rizzo, Janice Cheung, Rachel Lombardi, Peter Burke, Ken Segall, David Toledano and Rob Schoelkpof, all of whom have contributed to my "growth" one way or the other. On late long nights in the lab, Jim's vocal chords "assisted" by the sound from the cassette player in the background provided a source of company and recreation which was as important as the stimulating "noise" discussions I shared with Rob or the "going back to Solid State I" discussions with my office mates Stephan, Ken and Jens. Although I did not share any physics discussions with my first office mate, the "lovable obnoxious Turk" George Ugras, I did learn about the "finer" aspects of life and how often a pair of jeans should be washed in its lifetime. I consider myself lucky in the office mates I had and I thank them all for putting up with my tantrums.

During my tenure as the fridge "slave", I have had the good fortune of having Mandar Deshpande along with me to burn liquid Helium! Only aided by his calm presence and balanced approach did I manage to get some of those month long continuos runs successfully accomplished. Whye Kei besides being my co-practitioner of the essential food groups of graduate life [coffee, sugar, donuts, onion rings and coffee] provided a window beyond the world of physicists. In spite of being non-Proberites, both Mandar and WK could always be counted upon for help in the lab. I sincerely wish them both good luck !

Stanley Mroczkowski provided the insight and wisdom of a senior friend, and useful tips all along the way. Jayne Miller's efficiency and smile is what keeps the Applied Physics Dept. running smoothly. Pat (Brodka) with her kind warm disposition and an inexhaustible supply of candies helped me tide over the Yale beaureucracy, and more.

I would like to now thank those who have contributed towards an equally important part of my education, namely my personal growth (oh yes, its a debatable issue !). In particular, three people have especially made this journey possible. Stephan who provided me with a kick in the right place at the right time and failed in his efforts to induce alcohol intake, Bob (Wheeler), whose passion and energy lifted my spirits when all seemed lost, and whom I managed to get addicted to Willoughby's coffee, and my cousin sister Pooja, who in spite of being spatially so far away in India, through her unflinching love and trust in me, was close in thoughts, and taught me to value myself as a person.

Whatever I have achieved today, has its foundation in the love and sacrifice of my parents.

Table of Contents

Acknowledgments ii

List of Figures and Tables vii

List of Symbols and Abbreviations ix

1. Introduction 1

2. Background and Historical Overview 3

3. Theory of Heat Flow in GaAs 2DEGs 8

3.1 Introduction 8

3.2 Heat Flow via Phonon Emission 9

3.3 Heat Flow via Electron Diffusion 14

3.4 Heat Flow via Phonon Emission and Electron Diffusion 16

4. Samples 19

4.1 Design Considerations 19

4.2 Sample Fabrication from GaAs/AlGaAs heterostructures 21

4.3 Sample Characterization 25

5. Thermometry 27

5.1 Weak Localization as an Electron Thermometer 27

5.2 Sample Resistance as an Electron Thermometer 29

6. Experimental Apparatus and Techniques 32

6.1 Cryogenics 32

6.2 Sample Mount 33
6.3 Extraneous Sources of Power 34
6.4 Measurement Setup 35

7. Results and Analysis 41
7.1) Heat Flow Measurements 41
7.2) Electron-Phonon Scattering Rates 47

8. Conclusions 50

Appendix A: Numerical Simulation of Temperature Profile 52
Appendix B: Fabrication Notes 56
Appendix C: Weak Localization 61
Appendix D: Sample Mount in the Dilution Refrigerator 65

Bibliography 68

List of Figures and Tables

Figure		Page
2.1	Electron-phonon scattering regimes.	4
3.1	Schematic of a Hall bar with ends maintained at T_{mc}.	14
3.2	Simulation of temperature profile along the sample length.	17
3.3	P *vs.* T_e theory curves for sample A.	18
4.1	Optical mask layout for samples B.	20
4.2	Typical layer structure of a GaAs/AlGaAs heterostructure.	21
4.3	Schematic energy band diagram of a typical GaAs/AlGaAs heterostructure.	22
4.4	Optical image of sample B1.	25
4.5	Shubnikov-de Haas oscillations for sample B1.	26
5.1	2D weak localization data and fit.	28
5.2	Use of weak localization as an electron thermometer.	28
5.3	Use of sample resistance as an electron thermometer.	29
5.4	Change in resistance due to electron-electron interactions: data and fit.	30
6.1	Circuit for resistance measurements.	36
6.2	Resistance calibration using Landau level quantization.	38
6.3	Input noise of MN2311 preamplifier.	40
7.1	P *vs.* T_e data and theory for sample A.	41
7.2	P *vs.* T_e data and theory for sample B1.	42
7.3	P *vs.* T_e data and theory for sample B1 and B2: area dependence.	43
7.4	P *vs.* T_e data and theory for sample B1 and B3: area dependence.	44
7.5	Fourier Transform of R(1/B) for sample B1.	45
7.6	P *vs.* T_e data and theory for sample C.	46
7.7	$\tau_{e\text{-}ph}^{-1}$ *vs.* T_e data and fit for sample B1.	48
7.8	$\tau_{e\text{-}ph}^{-1}$ *vs.* l_{tr} data for sample B1.	48

D.1 Mixing chamber and sample mount of the dilution refrigerator. 66

D.2 Shielding and filtering of a sample lead. 67

Table Page

2.1 Electron-phonon scattering in GaAs 2DEGs below 30K. 6

4.1 Summary of device parameters. 26

5.1 Experimental and transport magnetic field for R *vs.* T_{mc}. 30

7.1 Transport mean free path and ql_{tr}. 47

List of Symbols and Abbreviations

$\propto$	Proportional to
$\approx$	Approximately equal to
2D	Two-dimensional
2DEG	Two-dimensional electron gas
B	Magnetic field
e	Electron charge
h	Planck's constant
$\hbar$	Planck's constant $\div 2\pi$
k	Electron wavevector
k_F	Electron Fermi wavevector
E_F	Electron Fermi energy
k_B	Boltzmann's constant
L	Lorenz number
γ	Sommerfeld constant
C_e	Electronic heat capacity
l	Electron elastic mean free path
l_{tr}	Electron transport mean free path
L_ϕ	Electron phase coherence length
q	Phonon wavevector
q_{typ}	Typical phonon wavevector
λ_s	Electron screening length
$\tau_{e\text{-}ph}$	Electron-phonon scattering time
$G_{e\text{-}ph}$	Electron-phonon thermal conductance
$P_{e\text{-}ph}$	Power flowing out of the 2DEG via phonon emission
$P_{e\text{-}diff}$	Power flowing out of the 2DEG via electron diffusion

n_s	Sheet density of electrons in the 2DEG including both spins
μ	Electron mobility
ρ	Sheet resistivity
R	Resistance
T_e	Electron temperature
T_{ph}	Phonon temperature
T_{mc}	Mixing chamber temperature
T_c	Characteristic crossover temperature between Equipartition and Bloch-Gruneisen regimes
s	Velocity of sound
PZ	Piezoelectric potential
DP	Deformation potential
WL	Weak localization
SO	Spin-orbit
SdH	Shubnikov-de Haas
LHe	Liquid helium
LIA	Lock-in amplifier
MBE	Molecular beam epitaxy
MC	Mixing chamber of the dilution refrigerator
NID	Not intentionally doped
RuO	Ruthenium oxide
mAh	mA hours
FT	Fourier transform

Chapter 1

Introduction

Electron-phonon scattering is one of the most fundamental processes in solids. In clean bulk metals, it has been well established that the electron-phonon energy relaxation rate, $\tau_{e\text{-}ph}^{-1}$, varies as T^3 at temperatures below the Debye temperature, θ_D. But our understanding in lower-dimensional and disordered systems is limited [Bergmann, 1990 and Gantmakher, 1987]. Experimental studies in metal films have yielded a range of different and conflicting results. Theoretical efforts to explain them have focused mainly on the following two issues.

The first issue for electron-phonon scattering in metal films is a modification to the T^3 dependence due to disorder. The results obtained with different theories do not agree [Takayama, 1973; Rammer 1973; Belitz, 1987] but it is now believed that the temperature dependence of $\tau_{e\text{-}ph}^{-1}$ should increase from T^3 to T^4 when the characteristic phonon wave vector q becomes less than inverse of the electron mean free path, l ($ql<1$) [Reizer, 1986]. Most experiments in dirty films, however, yield a different dependence close to T^2 [e.g., Bergmann, 1990; Gershenson, 1990, Pitsina, 1995].

The second issue in metal films is the modification to the phonon spectrum, which is three-dimensional for a bulk material. For a film thickness less than the typical phonon wavelength, and a large acoustic mismatch between the film and substrate, one expects a reduction in the effective dimensionality of the phonons [Belitz, 1987]. This leads to a reduced phase space for phonons, resulting in a $\tau_{e\text{-}ph}^{-1} \propto T^m$, where $2 \leq m \leq 3$. The same considerations may also lead to a non-Debye like phonon dispersion relation [Lifshitz, 1952]. Unfortunately, these theories also do not agree with most experimental findings [e.g., DiTiusa, 1992]. Furthermore, most metals have a non-spherical Fermi surface, which

implies a non-uniform density of states and non-scalar interaction potential. These features are harder to model theoretically.

A two-dimensional electron gas (2DEG) formed in GaAs at the interface of GaAs and AlGaAs from electrons in the lowest quantized subband offers much more of a model system in which to study the electron-phonon interaction in a two-dimensional electron system. The lattice matched heterostructure ensures that phonons are three dimensional. Since there is very little acoustic mismatch between GaAs and AlGaAs, the phonons emitted by the electrons are not trapped at the GaAs/AlGaAs interface. Therefore they are not trapped in the plane of the 2DEG and are able to thermalize with the bulk phonons in the lattice. The parabolic energy band for the 2DEG results in a circular Fermi surface, which is simpler to deal with theoretically. It is also easier to achieve desired amounts of disorder in such heterostructures as compared to metal films. One can thus systematically study the effects of reduced electron dimensionality and disorder on electron-phonon scattering.

We have studied the electron-phonon energy relaxation rate in a GaAs 2DEG and its dependence on disorder. Besides being of fundamental importance, this issue has important implications for low temperature transport experiments and applications. Chapter 2 presents an overview of the work on electron-phonon scattering rates in GaAs 2DEGs at low temperatures. Chapter 3 gives a theoretical treatment of the mechanisms of heat flow which are important at these temperatures. In the next chapter, we discuss the design and fabrication of samples keeping in mind the constraints imposed by the operating heat flow mechanisms. Chapter 5 deals with the techniques used to measure the temperature of the 2DEG. This chapter is followed by a detailed treatment of the experimental techniques and apparatus used. In Chapter 7, we discuss our experimental results and their analysis. Finally, we briefly summarize our experiments and discuss the implications of this work.

Chapter 2

Background and Historical Overview

The electron-phonon energy relaxation rate is often extracted from measurements of the energy transfer rate between the electron gas, assumed to be at a distinct temperature, T_e, and the lattice, maintained at T_{ph}. The net energy transfer rate, $P_{e\text{-}ph}$, is determined by the rate at which energy flows out of the electron gas by phonon emission, and the rate at which energy flows into the electron gas by phonon absorption from the lattice.

There are two types of interactions by which the electrons can exchange energy with phonons. A longitudinal acoustic phonon generates periodic spatial dilations as it propagates through a lattice, and causes the electron to scatter ineleastically as it moves from one region to another of slightly different periodicity. This phenomenon is known as Deformation Potential (DP) interaction, and occurs in all solids. Furthermore, if the lattice has oppositely charged ions with different masses which are displaced by different amounts as the phonon (longitudinal or transverse) propogates through the solid, then an additional electrical field with the periodicity of the phonon wavelength is created. The interaction of the electrons with this polarization field is what is known as Piezoelectric (PZ) coupling. In a polar semiconductor, the electrons and phonons interact both via Piezoelectric and Deformation Potentials. For $k_B T_e << E_F$, the net energy transfer rate for each contribution is given by

$$P_{e-ph} = \alpha\left(T_e^p - T_{ph}^p\right), \tag{2.1}$$

where α and p depend on the specific type of electron-phonon interaction, and α is proportional to the device area A. The relative magnitudes of the PZ and DP contributions

to the total energy transfer rate depend on the temperature range of interest. Whenever one type of interaction dominates, the energy relaxation rate is given by

$$\tau_{e-ph}^{-1} \equiv \left(\frac{G_{e-ph}}{C_e}\right) = \left(\frac{dP_{e-ph}/dT_e}{C_e}\right) = \left(\frac{p\alpha}{A\gamma}\right) T_e^{p-2} \qquad (2.2)$$

where $G_{e\text{-}ph}$ is the thermal conductance due to phonon emission for the dominant interaction, and $C_e = A\gamma T_e$ is the electronic heat capacity of the electron gas, with γ the Sommerfield parameter per unit area.

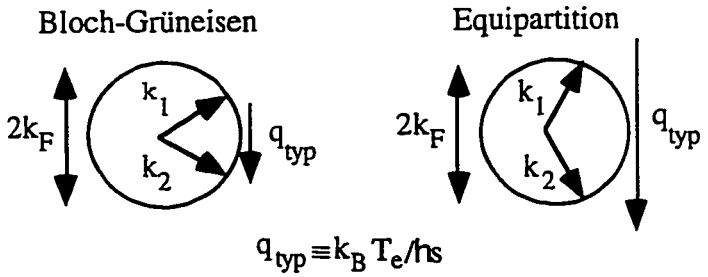

Figure 2.1 Electron-phonon scattering regimes based on q_{typ} being less or greater than the diameter of the Fermi sphere ($2k_F$).

The electron inelastic scattering time is the typical time it takes the electron to relax to the Fermi energy from a state $k_B T_e$ higher in energy. In an electron-phonon scattering event, an electron in state k_1 can possibly relax its energy by $k_B T_e$ to go to a state k_2, by emitting an acoustic phonon with a wave vector $q_{typ} \equiv k_B T_e/\hbar s$, where s is the velocity of sound. At the low temperatures of interest (<30K) in 2D semiconductor systems, two major temperature regimes can be distinguished based on the size of q_{typ} ($\approx 0.5 \cdot 10^8\ T_e$ [$m^{-1}K^{-1}$]) compared to the diameter of the Fermi circle, $2k_F$ ($\approx 5 \cdot 10^8\ n_s^{1/2}$ [m^{-1}] where n_s is the electron density in units of 10^{16} m^{-2}). At low electron temperatures, where $q_{typ} < 2k_F$, an electron can relax its energy by an amount $k_B T_e$ by emitting a single phonon. At higher temperatures, where $q_{typ} > 2k_F$, momentum conservation requires that the electron has to emit multiple phonons with $q < q_{typ}$ to relax its energy by $k_B T_e$. The crossover between

these regimes occurs at a characteristic temperature, T_c, which lies between 3-10K for GaAs. The temperature regime above T_c is known as the equipartition regime, and that below it as the Bloch-Grüneisen regime.

The Bloch-Grüneisen regime can be further divided into two regimes based on how well the electrons screen the electron-phonon interaction. Suppose a positively charged particle is fixed at a given position in an electron gas. It will attract electrons, creating a surplus of negative charge in its neighborhood, which reduces (or screens) its electric field. In a similar fashion, the electric field created by the phonons will be screened by the electron gas. There is an effective distance beyond which the effect of the electric field is no longer felt i.e. the field is strongly screened. This distance is known as the screening length λ_s. At the high temperature end of the Bloch-Grüneisen regime, the phonon wavelength is much smaller than λ_s and the electron-phonon interaction is unscreened. As the temperature is lowered, the phonon wavelength increases until it exceeds the electron screening length λ_s (or $q_{typ}\lambda_s < 2\pi$) leading to the screened Bloch-Grüneisen regime at the lowest temperatures. In this regime the strength of the electron-phonon coupling is reduced because of screening. This occurs below 1K in GaAs.

As an aside, in a metal the Fermi energy is much larger than in a 2DEG. Therefore in a metal, k_F is much greater than the maximum phonon wave vector, which is of order q_{Debye}. Thus, in a metal an electron can always relax its energy by emitting a single phonon. The Bloch-Grüneisen regime in metals occurs when $T_e << \theta_D$.

For a 2DEG in the equipartition regime, both PZ and DP interactions are predicted to result in p=1 in eq. 2.1 [Price, 1982]. In GaAs, the predominant interaction is DP, with PZ typically adding just 10% of the DP contribution [Price, 1982]. In the unscreened[1] Bloch-Grüneisen regime, it is predicted that p=3 and 5 respectively for PZ and DP interactions

[1] Strictly speaking, some screening always exists. But it is so weak in the so called unscreened Bloch-Grüneisen regime that the screening function is unity. In comparison, in the screened Bloch-Grüneisen regime, the screening function is directly proportional to q (eq. 3.5). This is what leads to a difference in temperature dependence proportional to T_e^2 between the two regimes.

[Karpus, 1988]. In the screened Bloch-Grüneisen regime one expects p=5 and 7 for the PZ and DP interactions respectively [Price, 1982; Karpus, 1988]. The screened PZ interaction is expected to dominate below 1K in GaAs. Thus, the p=5 dependence of the screened PZ contribution leads to a T^3 dependence for the electron-phonon scattering rate in GaAs as a limiting low temperature behavior. Because of the relative magnitudes of the DP and PZ contributions, the low temperature behavior of $\tau_{e\text{-}ph}^{-1} \propto T^3$ extends to somewhat higher temperatures than is expected from the screened piezoelectric contribution alone.

Regime	Criterion	Crossover T_e	Interaction Type	p
Equipartition	$q_{typ} > 2k_F$		PZ	1
			DP	1
		$T_c \approx$ 3-10K		
Bloch-Grüneisen (unscreened)	$q_{typ} < 2k_F$		PZ	3
	$q_{typ}\lambda_s > 2\pi$		DP	5
		$T \approx$ 1K		
Bloch-Grüneisen (screened)	$q_{typ} < 2k_F$		PZ	5
	$q_{typ}\lambda_s < 2\pi$		DP	7

Table 2.1 Electron-phonon scattering in GaAs 2DEGs below 30K (for n_s ranging from 10^{15} m^{-2} to 10^{16} m^{-2}).

Most experiments [Hirakawa, 1986; Blyumina, 1986; Kreschuk, 1988; Ma, 1991; Ridley, 1991 and Verevkin, 1996] in GaAs 2DEGs in the temperature range 2K<T<12K find p=3. This appears to result from the unscreened PZ interaction. Note that the above predictions for GaAs 2DEGs are valid only for a singly occupied subband. As the 2nd subband begins to be occupied, Kreschuk *et al.* [Kreschuk, 1988] see the p=3 behavior change to p=2, although Ma *et al.* [Ma, 1991] do not see such a change. Nonetheless, both find an increase in the energy relaxation rate because of inter subband scattering.

No conclusive experimental results on the limiting low temperature behavior appropriate to screened piezoelectric coupling are available in the literature. Wennberg *et al.* [Wennberg, 1986] have seen the expected dependence of p=5 for T ≤ 1K in a multiple-

quantum-well heterostructure. Their measured prefactor is smaller than the predicted value by two orders of magnitude. In our experiments, we have measured electron-phonon energy relaxation rate in this regime, in a single 2DEG in a GaAs/AlGaAs heterostructure. We also explore how the electron-phonon scattering rate changes with the electron mean free path at these low temperatures.

Most investigations of the electron-phonon scattering rate are based on quantum corrections to electronic conductivity due to electron-phonon interaction. The first uses weak localization [see Chapter 5 for details] to determine the phase-breaking rate [Santhanam *et al.*, 1987] with $T_e \approx T_{ph}$. At high temperatures, the phase-breaking rate is approximately equal to the electron-phonon scattering rate [Hikami *et al.*, 1980]. However, at low temperatures electron-electron dephasing dominates, and extracting $\tau_{e\text{-}ph}^{-1}$ becomes difficult. The second method uses the temperature dependence of the mobility to extract the scattering rate, but is affected by screened Coulomb scattering and quantum corrections at low temperatures.

In the present study we utilize electron heating which is sensitive only to energy relaxation mechanisms, and is thus a more direct measurement of the electron-phonon energy relaxation process. Power dissipated in the electron gas raises its temperature above the phonon temperature. The hot electrons can relax to lower temperatures by phonon emission. In long samples, the average temperature rise is proportional to $\tau_{e\text{-}ph}$ for small input power levels. At low temperatures, electron out-diffusion can provide a competing mechanism for heat flow. In order to understand the relative importance of the two mechanisms, we look at the theory behind the two mechanisms in the following chapter.

Chapter 3

Theory of Heat Flow in GaAs 2DEGs

3.1) Introduction

The electrons in a 2DEG and the phonons in the lattice of a GaAs/AlGaAs heterostructure are assumed to be in thermal equilibrium with each other at room temperature. This is justified because the thermal conductance between them is high. But as the temperature is lowered, this thermal conductance starts decreasing. In the temperature regime of interest (i.e., below 0.5K) the thermal conductance becomes so small that even power levels below 1 pW can raise the temperature of the electron gas above that of the phonons in the lattice. Then the electron and phonon subsystems each of which is assumed to be in an internal equilibrium, become decoupled and have a distinct temperature. In the present context, the lattice phonons are maintained at the dilution refrigerator mixing chamber temperature (see Chapter 6). The electrons, however, are potentially at a higher temperature T_e because of some power which couples to the 2DEG. This power could come from an applied electric field or from some extraneous source (see Chapter 6). Implicit in the assumption of a constant T_e is that electron-electron interactions are sufficiently strong to ensure rapid equilibrium within the electronic system of the energy extracted from the external electric field.

The hot electrons can relax to lower temperatures by two mechanisms. The first is by emitting phonons which thermalize with the lattice phonons. The second is by electron diffusion. Hot electrons diffuse out to the cold ohmic contacts to be replaced by cold electrons. Let us examine the theories behind these mechanisms in order to understand their relative importance in the temperature regime of interest.

3.2) Heat Flow via Phonon emission

As discussed in Chapter 2, below 1K in the screened Bloch-Grüneisen regime, piezoelectric interaction is the dominant mechanism for electron-phonon scattering. We estimate the power flowing out by this mechanism by a theory put forward by Price [Price, 1982], which predicts

$$P_{e-ph} \approx 1.65 \times 10^6 n_s^{-1/2} A_{device} (T_e^5 - T_{ph}^5) \text{ [J/s]}, \qquad (3.1)$$

where n_s and A_{device} are the 2DEG density and area. This result is valid specifically for a single-subband $Al_{0.3}Ga_{0.7}As/GaAs$ heterojunction. It has been derived using the static screening formalism in the clean limit. Karpus [Karpus, 1988] finds the same temperature dependence as Price, but predicts that $P_{e\text{-}ph}$ is a factor of two smaller in magnitude. Our calculations[1] following Price's formalism agree with Karpus's conclusion. Equation 3.1 gives the corrected value, which is half of the prediction in Price's paper. None of these theories [e.g., Price, 1982; Karpus, 1988] take into account the effects of impurities on the electron-phonon interaction.

Only very recently Chow *et al.* [Girvin, S., private communication; Chow *et al.*, submitted to Phys. Rev. Letters, 1996] have considered the effects of disorder. Their theory is in the hydrodynamic limit where typical phonon wave vectors and frequencies are negligible compared to the length scales over which conductivity varies. This happens in samples which are at very low temperatures and in high magnetic fields or if they are very disordered ($q_{th} l_{tr} << 1$). Chow *et al.* predict that the power flowing out to be

[1]We find that Price has a numerical error in his calculations, which account for the factor of 2. Prof. Steve Girvin has repeated his calculation and finds the same error [private communication].

$$P_{e-ph_{hydrodynamic}} = 6.75 \times 10^{-2} \frac{e^2 \rho}{h} A_{device} T_e{}^4 \quad [\text{J/s}]. \tag{3.2}$$

Our measurements have been performed in low magnetic fields, and our samples were not disordered enough to enter the hydrodynamic regime. Therefore, this theory does not apply to our experiments. We will discuss this issue in greater detail in Chapter 7.

The Price prediction in the clean limit can be derived in a simple fashion. Consider a thin 2D electron layer assumed to be at a temperature T_e. In the temperature regime of interest, the electrons relax to a lower temperature by emitting 3D acoustic phonons induced by piezoelectric scattering. For simplicity, let us assume that the phonons are at 0K. This essentially sets the power absorbed by the 2DEG from the phonons to zero.

Let k be the electron wave vector in the plane of the 2DEG, which is assumed to be the x-y plane, and Q be the 3D phonon wave vector. If an electron in state k_1 is scattered to a state k_2, then momentum conservation in the x-y plane restricts the allowed values of k_2 to $k_2 = k_1 - q$, where q is the phonon wave vector in the x-y plane. But the total phonon wave vector Q is given by $Q = q + q_z$, where q_z is the phonon wave vector in the direction perpendicular to the 2DEG. Note that the electron momentum in the z direction is conserved to within Heisenberg's uncertainty principle. Since the electron wavefunction in real space is peaked very sharply in the z direction, it can readily absorb any momentum which is imparted by a phonon in that direction. But for purposes of energy conservation, one still has to consider the total phonon wave vector, Q, such that

$$E_{k_1} - E_{k_2} = \hbar\omega(Q) = \hbar s Q, \tag{3.3}$$

where s and $\omega(Q)$ are the velocity of sound and the acoustic phonon frequency. Even if we had not assumed the phonons to be at 0K, as long as $T_{ph} < \theta_D$, we only need consider acoustic phonons, and thus a simple linear dispersion relation.

If θ is the angle at which the electron is scattered from state k_1 to state k_2, then $q^2 = k_1^2 + k_2^2 - 2k_1k_2\cos\theta$. In the low temperature limit ($T_e < 0.5K$), $q << k_F$ and $|k_1| \approx |k_2| \approx k_F$, so that $q \approx k_F\theta$.

For piezoelectric scattering, the square of the electron-phonon interaction matrix elements are given [Manion, 1987] by

$$|M_l(Q)|^2_{3D} = \frac{\hbar(eh_{14})^2}{2\rho s_l}\frac{9q_z^2q^4}{2Q^7} \quad \text{and} \quad |M_t(Q)|^2_{3d} = \frac{\hbar(eh_{14})^2}{2\rho s_t}\frac{8q_z^4q^2+q^6}{2Q^7}, \tag{3.4}$$

where eh_{14} is the piezoelectric potential (≈ 0.12 eVÅ^{-1}), s_l is the longitudinal velocity of sound ($\approx$ 5240m/s), s_t is the transverse velocity of sound ($\approx$ 3070 m/s) and ρ is the mass density ($\approx$5.36 g/cm^3) for GaAs. Note that these squared matrix elements have a wave vector dependence proportional to Q^{-1} as compared to those for deformation potential coupling, which are proportional to Q. Since Q is proportional to T_e [eq. 3.12], this leads to a difference in temperature dependence proportional to T_e^2 for the ratio of electron-phonon scattering rates due to deformation potential and piezoelectric coupling.

In the temperature regime below 0.5K, $q << q_{TF}$ ($\approx 2\text{x}10^8$ /m), the Thomas-Fermi screening wave vector, and the interaction will be strongly screened. The effect of screening on the electron-phonon interaction can be introduced [Price, 1981] by multiplying the matrix elements by the static screening function for this system[2] [Stern, 1967]

$$\left|\frac{1}{\varepsilon}\right| \approx \frac{q}{q_{TF}}. \tag{3.5}$$

[2]Note that this is unlike a 3D metal where the screening function is proportional to $(q/q_{TF})^2$.

Using Fermi's Golden Rule and summing over all allowed states, the power flowing out of the 2DEG per unit area via phonon emission can now be written as

$$P_{e-ph} = 2\sum_{\lambda}\int\frac{d^2k_1}{(2\pi)^2}\int\frac{d^2k_2}{(2\pi)^2}\frac{2\pi}{\hbar}f(E_{k1})\left[1-f(E_{k2})\right]\int\frac{dq_z}{2\pi}\hbar\omega_\lambda(Q)\times \\ |M\lambda(Q)|^2_{3D}\frac{q^2}{{q_{TF}}^2}\delta(E_{k1}-E_{k2}-\hbar\omega_\lambda(Q)) \tag{3.6}$$

where the factor of 2 is due to spin, λ represents the longitudinal and transverse modes of the phonons, the first two integrals from the left are over the initial and final electron wave vectors and the Fermi functions denote the occupation probabilities in the initial and final k states. For each phonon wave vector q which is emitted, there is an allowed scattering for all q_z. This is represented by the integral over q_z. The delta function ensures energy conservation and $\hbar\omega(Q)$ represents the energy of the emitted phonon.

In order to simplify eq. 3.6, we define the density of single spin electron states, η, as

$$\eta \equiv \int\frac{d^2k_i}{(2\pi)^2}\delta(E-E_{ki}). \tag{3.7}$$

Eq. 3.6 can now be recast as

$$P_{e-ph} = \frac{2\eta^2}{{q_{TF}}^2\hbar}\sum_{\lambda}\int dE\int dq_z f(E)\left[1-f(E-\hbar\omega_\lambda(Q))\right]\hbar\omega_\lambda(Q)|M\lambda(Q)|^2_{3D}. \tag{3.8}$$

In this step we have used the fact that the energy density of states for the 2DEG is a constant. This is true only because for our experimental system, the Fermi surface is a circle. This assumption breaks down for most real metals. We can now use the identity

$$\int dE f(E)\left[1-f(E-\hbar\omega_\lambda(Q))\right]=\hbar\omega_\lambda(Q)n_B(\hbar\omega_\lambda(Q)), \tag{3.9}$$

where n_B is the phonon occupation number, and the following mathematical trick

$$1=\frac{1}{2\pi}\int_{-\pi}^{\pi}d\theta=\frac{1}{\pi}\int_{0}^{\pi}d\theta\approx\frac{1}{\pi k_F}\int_{0}^{\infty}dq \tag{3.10}$$

to obtain

$$P_{e-ph}=\frac{\eta^2}{\pi^2 {q_{TF}}^2\hbar k_F}\sum_\lambda\int d^3Q\,\left[\hbar\omega_\lambda(Q)\right]^2 n_B(\hbar\omega_\lambda(Q))\left\{|M_\lambda(Q)|^2_{3D}q\right\}. \tag{3.11}$$

To extract the temperature dependence, we define a new dimensionless energy X as

$$X\equiv\frac{\hbar s_\lambda Q}{k_B T_e}. \tag{3.12}$$

Note that the factor in the curly bracket is proportional to q/Q, and thus does not contribute to any temperature dependence. Factoring out the temperature dependent part, we obtain

$$P_{e-ph}=\frac{\eta^2}{\pi^2 {q_{TF}}^2\hbar k_F}\sum_\lambda\left\{|M_\lambda(Q)|^2_{3D}q\right\}\left(\frac{(k_B T_e)^5}{(\hbar s_\lambda)^3}\right)\int_0^\infty d^3X X^2\frac{1}{e^X-1}. \tag{3.13}$$

The integral can be solved yielding $4\pi\cdot 4!\cdot\xi_5$, where ξ is the Riemann zeta function and $\xi_5\approx 1.037$. The matrix elements with the λ summation can be evaluated by changing to angular coordinates. Using the required material constant values listed before and the relation $k_F=\sqrt{(2\pi n_s)}$ for a 2DEG, we finally obtain

$$P_{e-ph}/A_{device}\approx 1.65\times 10^6 n_s^{-1/2}T_e^5, \tag{3.14}$$

which is what Karpus predicts for phonons at 0K. Following a treatment similar to the one outlined above, one can obtain an expression for the power absorbed by the 2DEG identical to the one for the power emitted by the 2DEG, except that it will be proportional to T_{ph}^5 and not T_e^5. The difference of the two expressions gives the Price result. Note that the power flowing out via phonon emission scales with the device area, and has a temperature dependence proportional to T_e^5.

As an aside, in 3D metals also one finds that the power flowing out by phonon emission at the lowest temperatures follows a temperature dependence proportional to T_e^5 [Ziman, 1979]. But this is due to the screened DP interaction in metals. In semiconductors the screened DP interaction is weaker than in metals and leads to a temperature dependence proportional to T_e^7 for the heat flowing out due to phonon emission.

3.3) Heat Flow via Electron Diffusion

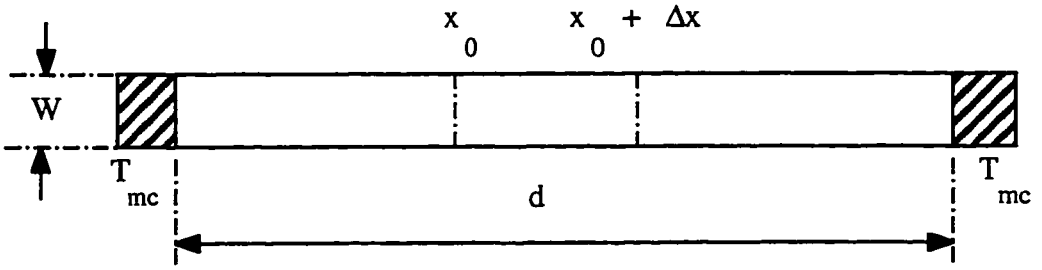

Figure 3.1 Schematic of a Hall bar with ends maintained at T_{mc}.

In order to calculate the heat flowing out via electron diffusion, let us consider a 2DEG in the shape of a Hall bar with its end ohmic contacts maintained at the mixing chamber temperature, T_{mc}. Using the Wiedemann-Franz law, we can relate the 2D electrical conductivity σ of the 2DEG to the 2D thermal conductivity κ at a given electron temperature T as

$$\frac{\kappa}{\sigma T} = \frac{\pi^2}{3}\left(\frac{k_B}{e}\right)^2 \equiv L \qquad \left[\frac{J\Omega}{sK^2}\right], \tag{3.15}$$

where L is known as the Lorenz number[3]. If a current I flows through the electron gas, then we can assume uniform ohmic heating along its length d and the heat flow equation for a segment Δx in steady state can be written as

$$I^2\rho\frac{dx}{W}=\frac{L}{\rho W}\left\{\left(T\frac{dT}{dx}\right)_{x_0}-\left(T\frac{dT}{dx}\right)_{x_0+\Delta x}\right\}. \tag{3.16}$$

Solving (3.16) for T(x), we get

$$T(x)=\left(T_{mc}{}^2+\left(\frac{I\rho}{W}\right)^2\frac{xd}{L}-\left(\frac{I\rho}{W}\right)^2\frac{x^2}{L}\right)^{1/2}. \tag{3.17}$$

This can be used to calculate the temperature profile along the length of the sample for different measuring currents and sample parameters when heat flows out via only electron diffusion. Further, solving (3.17) for the peak temperaturethe $T_e \equiv T(x = d/2)$, and rearranging terms, we can now express the power flowing out of the 2DEG via electron diffusion as

$$P_{e-diff}=\frac{4L}{R}\left(T_e{}^2-T_{mc}{}^2\right)\approx\frac{10^{-7}}{R}\left(T_e{}^2-T_{mc}{}^2\right)\text{ [J/s]}. \tag{3.18}$$

Note that the power flowing out via e-diffusion decreases with increasing resistance. For a 2D system, resistance is simply resistivity times the number of squares (ratio of length upon width ie. d/W). The longer the sample, the more time it takes for the electrons to diffuse out, and hence smaller the thermal conductance due to electron diffusion. In contrast, the power flowing out via phonon emission scales with the device area (d·W).

[3]Our derivation confirms that eq. 3.15 is independent of dimensionality of the electronic system.

Also for heat flow via electron diffusion, the power flowing out has a temperature dependence proportional to T_e^2 as compared to T_e^5 for the phonon case. Thus, one would expect phonon emission to dominate at higher temperatures.

3.4) Heat Flow via Phonon Emission and Electron Diffusion

Under typical experimental conditions, heat is carried away both by electron diffusion and phonon emission. To estimate the relative contribution of each mechanism, we can simply add another heat sink term corresponding to heat flow by phonon emission into equation 3.16. Rearranging terms, we get

$$\frac{-L}{2\rho}\frac{d^2T(x)^2}{dx^2} + \frac{1.65\times10^6}{\sqrt{n_s}}T(x)^5 = \frac{I^2\rho}{W^2} + \frac{1.65\times10^6}{\sqrt{n_s}}T_{mc}{}^5. \qquad (3.19)$$

Eq. 3.19 can now be solved numerically[4] to obtain the temperature profile along the length of the sample for a given input power. Since ρ changes by at most 1% over the whole experimental temperature range, it has been taken to be temperature independent for purposes of heat dissipation calculation in the 2DEG.

Figure 3.2 shows the temperature along the length of the sample as a function of input power. At lower current levels, the heat flow is dominated by electron diffusion and the electrons in the center of the Hall bar are hotter than those near the ohmic contacts. The temperature profile in this case has a functional form close to square root of a parabola, as expected from eq. 3.17. As the input current increases, more heat is carried out by phonon emission and the electrons start to attain a uniform temperature along the sample length. Even when the dominant mechanism of heat flow is electron out diffusion, the temperature

[4]A program has been written which can simulate the temperature profile along the sample length as a function of input current or any of its parameters. See Appendix A.

profile is flat near the center. Hence, we measure the central region of our samples, which corresponds to the peak temperature T_e in our formulae.

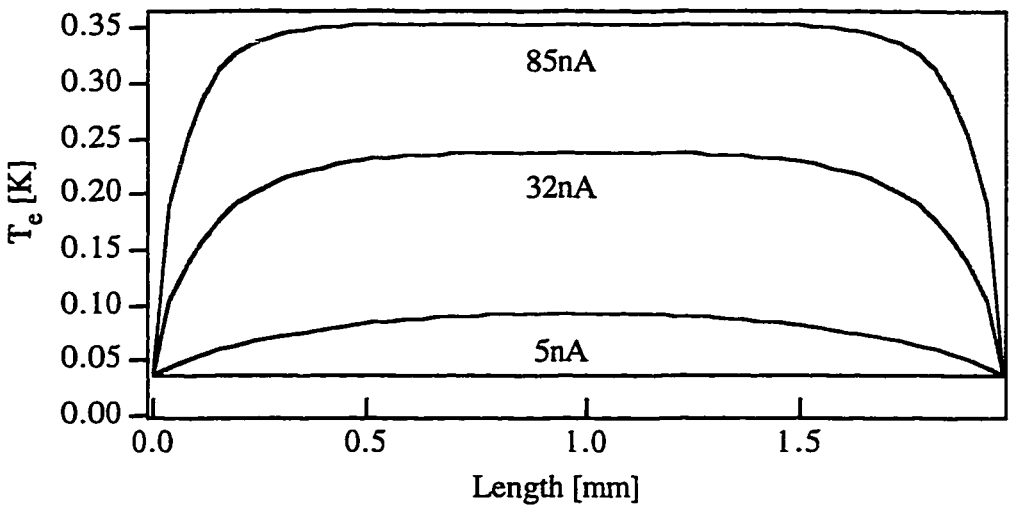

Figure 3.2 Simulation of temperature profile along the length of the sample for typical parameters.

We can solve 3.19 to obtain temperature profiles as a function of input current. We can then plot the total power flowing out of the 2DEG including both mechanisms of heat flow as a function of the peak temperature, T_e. The dark solid line in Figure 3.3 shows such a heat flow solution for Sample A (see Table 4.1 for description of sample parameters), with T_{mc} = 36mK. The individual contributions from phonon emission and electron diffusion are also plotted in the same graph. Note that for a given T_e, a simple addition of the power flowing out via each mechanism operating by itself gives us almost[5] the same total power flowing out as that obtained from the numerical solution of eq. 3.19 which includes both the mechanisms operating simultaneously. This shows that the two mechanisms operate essentially in parallel.

[5]The agreement is within 1% of the values, and improves with the use of a finer grid in the simulation.

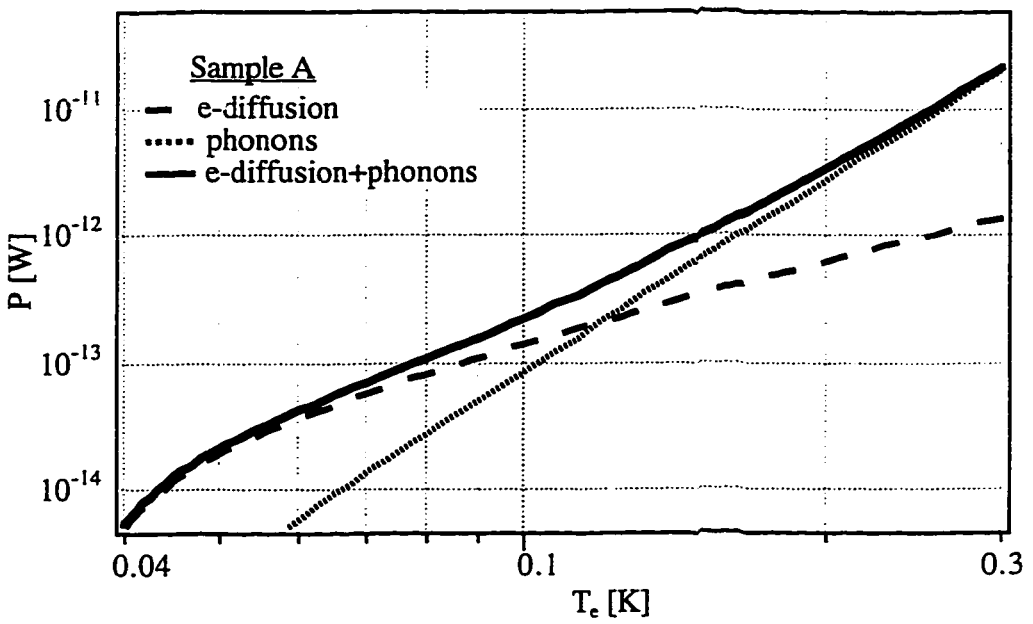

Figure 3.3 The power flowing out of the 2DEG as a function of its peak electron temperature at a fixed mixing chamber temperature of 36mK. The solid line represents the total power flowing out and the dashed lines represent contributions from heat flow via phonon emission and electron out diffusion.

As can be seen from the above figure, at lower temperatures, most of the heat flows out via electron diffusion, while phonon emission starts to dominate at higher temperatures. The crossover between the two mechanisms, dependent on sample parameters, is typically around 100mK. In the next chapter, we discuss how to design a sample such that the dominant heat flow mechanism is phonon emission.

Chapter 4

Samples

4.1) Design Considerations

In order to measure the energy relaxation rate due to phonon emission in the temperature regime below 500 mK, the sample has to be designed such that the heat flow is dominated by phonon emission rather than electron diffusion. The sample geometries were chosen to satisfy this criterion, constrained by the available wafer parameters and the background power level in our experimental setup (see Chapter 6). Important design issues considered were:

- Large area devices, typically of the order of 0.1 mm^2, were made to ensure that phonon emission dominates over electron diffusion.
- The sample dimensions (Table 4.1) and distances between the measurement probes were designed to be larger than the relevant microscopic length scales in the experiment, such as the electron mean free path and the electron phase coherence length. This ensures that the 2DEG is a truly 2D diffusive system, and even in the presence of uniform heating there exists a well defined local electron temperature.
- The voltage leads were patterned in the 2DEG itself and were made long and narrow to ensure that they have a high thermal resistance, and hence do not perturb the temperature of the sample. Even in the case of the smallest sample (see Figure 4.3), the number of squares for each voltage lead was more than twice that for the device, while their area was less than half the device area.
- The voltage leads were placed in the center of the sample in order to infer the peak electron temperature as discussed in Chapter 3.

The samples were designed to test the dependence of heat flowing via phonon emission on the device geometry. Figure 4.1 shows a layout of the optical mask for samples B. The black regions represent the ohmic contacts and the shaded regions the 2DEG. Samples B1 and B3 have the same area, but different number of squares so that they have the same heat flow provided phonon emission is the dominant mechanism for energy relaxation. Sample B1 has about 9 times larger area than sample B2 to test if the heat flow out due to phonon emission scales with the device area, and the same number of squares in order to ensure identical contributions of heat flow due to electron diffusion.

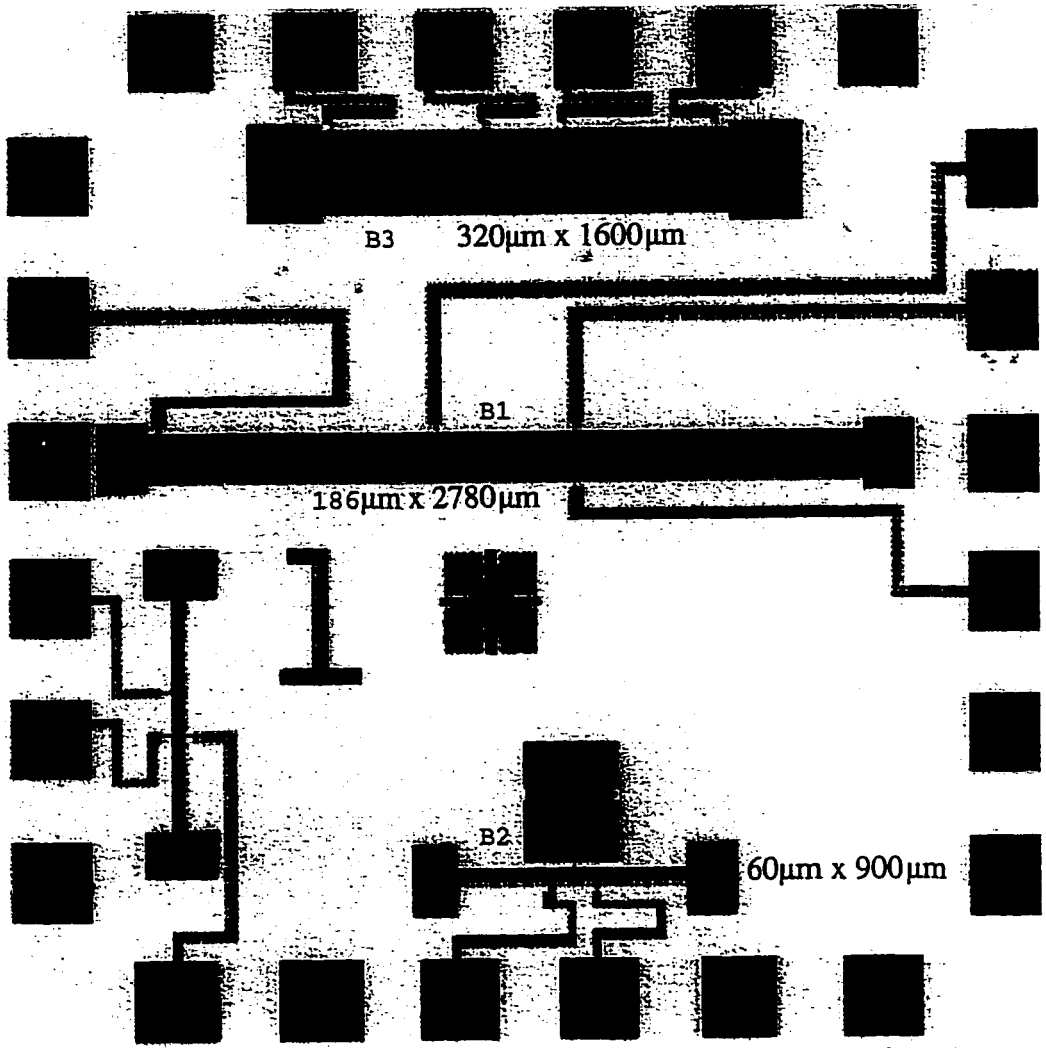

Figure 4.1 Layout of the optical mask for samples B. The black regions represent the ohmic contacts and the shaded regions the 2DEG. The actual device dimensions are labelled. The voltage leads narrow down to typically 4μm x 40μm towards the Hall bars.

4.2) Sample Fabrication From GaAs/AlGaAs Heterostructure

A cross-sectional view of a typical GaAs/$Al_xGa_{1-x}As$ heterostructure is shown in Figure 4.2. Starting from a substrate wafer of semi-insulating GaAs, a thick layer of undoped GaAs is grown first. This is followed by a spacer layer of undoped AlGaAs, then a layer of AlGaAs doped with Si, and finally a thin cap layer of GaAs to protect the reactive AlGaAs layers. The Al fraction, x, is usually close to 0.3. The heterostructures used in this work were grown by Dr. Bob Sacks at United Technologies Research Center in East Hartford, CT who is now at Ohio State University.

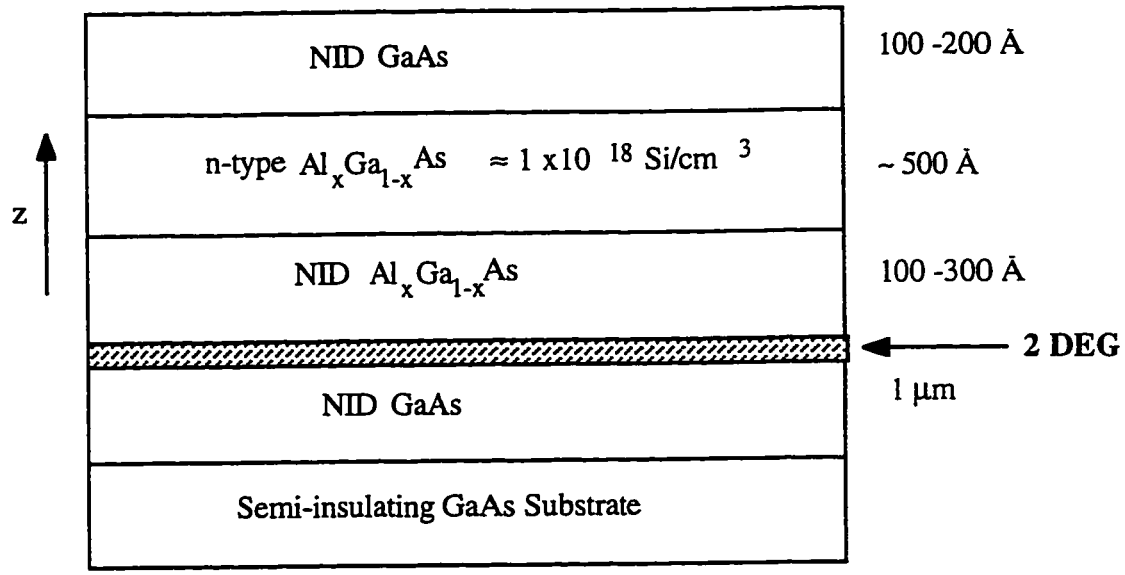

Figure 4.2 Typical layer structure of a GaAs/$Al_xGa_{1-x}As$ heterostructure (NID stands for not intentionally doped).

The energy band diagram shown in Figure 4.3 [modified from Keller, 1995] shows the formation of the 2DEG at the interface of undoped GaAs and AlGaAs layers. The discontinuity in the conduction band between these two materials results in a narrow potential well in the z direction with discrete energy levels that define the bottom of the 2D subbands. The n-type dopants in the AlGaAs provide electrons which fill up these bands. By controlling the spacer layer thickness and the doping concentration, one can achieve the desired electron density and populate just the lowest subband. The mobility[1], too, can be

[1] After a certain spacer layer thickness, the mobility is determined by the unintentional impurities in GaAs, rather than the donors and is hence determined by the cleanliness of the growth chamber.

controlled by adjusting the spacer layer thickness since it spatially separates the main source of scattering, the charged donors in the doped AlGaAs layer, from the plane of the 2DEG. Thus this experimental system offers the advantage of a 2D layer of electrons whose density and mobility can be chosen as desired.

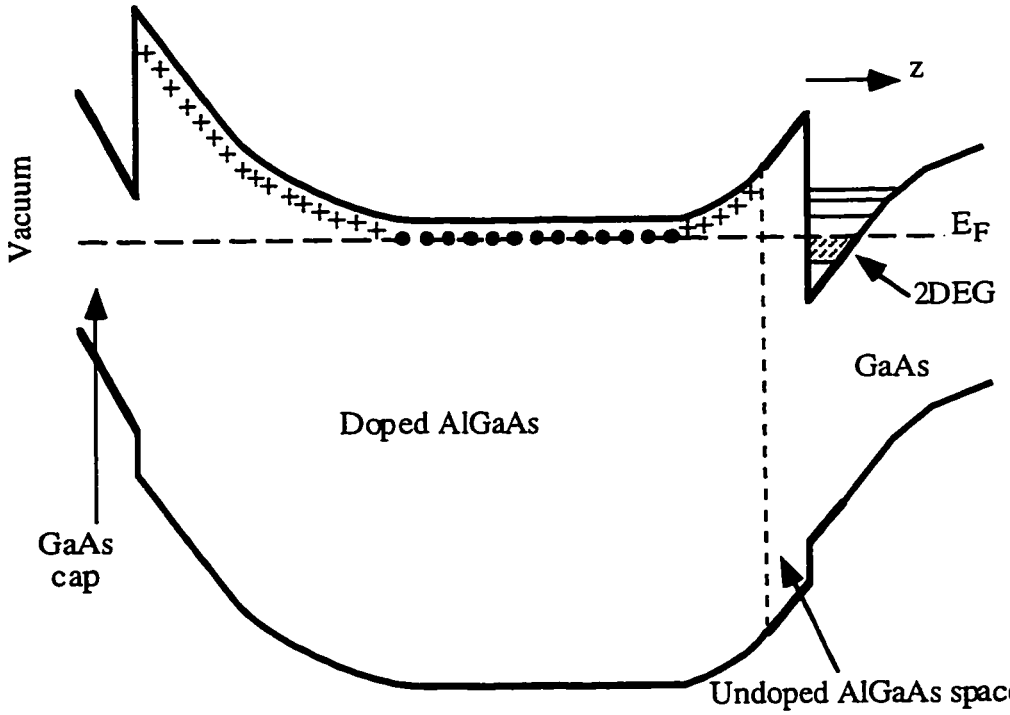

Figure 4.3 Schematic energy band diagram of a typical GaAs/AlGaAs heterostructure. The ionized donors (indicated by +) provide the electrons in the 2DEG formed in the triangular potential well shown on right. The discrete lines depict the bottoms of the 2D subbands.

The heterostructures were patterned at the Yale Microfabrication Facility using the conventional photolithography, shallow wet etch and metal liftoff processes. Chrome on quartz optical masks were used to define the ohmic contact, gate and 2DEG patterns.

The first major processing step was to form ohmic contacts to the 2DEG in the GaAs/AlGaAs heterostructure. This was done by evaporating Ni, Ge and Au onto its surface and annealing the sample to diffuse the metal into the wafer. The diffused metal is believed to migrate into the wafer in irregular spikes and contact the 2DEG [Braslau, 1981]. These alloyed NiGeAu contacts are notorious in the low temperature community for

failing to work properly at low temperatures and large magnetic fields. They often become noisy and their resistance increases as much as two orders of magnitude on cooling from room temperature to liquid He temperatures. Trying to resurrect them by forcing high currents through them or repeated annealing is not always successful, and sometimes damages the sample. Sometimes, even if contacts behave ideally at low temperatures, they can display negative resistance at large magnetic fields [for details, see Richter, 1993].

It was essential in our experiments to have low resistance ohmic contacts to ensure that their thermal conductance due to electron diffusion was high, and hence they were at a temperature close to that of the cryostat's cold bath. At present, the art of making good low temperature ohmic contacts to a GaAs/AlGaAs 2DEG is more of an alchemy than an exact science. It is believed that when the temperature rises during annealing, the AuGe alloy begins to melt and Ga diffuses into the Au. This frees Ga sites in the crystal to be occupied by Ge which acts like a n-type dopant. Ni is supposed to aid in the diffusion of Ge, but is mainly supposed to help the metal stick to the surface of the wafer. The following steps were taken to improve the low temperature performance of the ohmic contacts:

- The thickness of Ge layer deposited was increased by a factor of 2.5, while that of Au and Ni was increased by a factor of 1.5.
- Care was taken to see that there are no p-type impurities in the thermal evaporator or in the chamber of the rapid thermal annealer. The quartzware of the annealer was etched in $HF:HNO_3$ to remove any impurities.

After these changes, low temperature contacts with 30Ω contact resistance for an area of $100\mu m^2$ were obtained with 75% device yield. A positive (though not guaranteed) signature of a good ohmic contact was when the post anneal metal looked dull with lot of uniform bubbles (e.g., see Figure 4.3). This is attributed to evolution of As gas during the high temperature anneal. However, it was found that bonding to such a surface was difficult. While depositing even more gold during the NiGeAu evaporation solved the

bonding problem, it caused the contact resistance to increase and made the I-V's non linear. This could happen if there is excess Au which getters more Ga than there is Ge available to replace it. The resulting Ga vacancies can cause a high resistance region [Robinson, 1975]. This issue was resolved by depositing a post anneal cap layer of Au.

To pattern the 2DEG, we used what is known as the shallow wet etch technique. In this technique the desired pattern is created in a mask material that resists the etch solution and then transferred to the sample material by simply immersing the sample in the etch solution for an appropriate time. It is clear that etching through the plane of the 2DEG will ensure good confinement of electrons in the desired region. However, in the shallow wet etch technique, one just removes the cap GaAs layer and some of the doped AlGaAs layer, and yet one achieves good electrical confinement at low temperatures. This technique has the advantage of causing no damage in the plane of the 2DEG, and is particularly useful for fabrication of submicron structures [Lee *et al.*, 1991; Ismail *et al.*, 1991].

The final step involved patterning and depositing gate metal on the GaAs cap layer. The metal-GaAs interface acts as a Schottky barrier which may be used to isolate the charges on the gate from the charges in the 2DEG. The system then essentially acts like a parallel plate capacitor, and the electron density in the 2DEG can be controlled by applying a gate voltage. This is a relatively straightforward process and the popular combination of metals is Ti-Au (Ti for sticking purposes and Au for conduction). But this gating process can lead to mobility degradation [Dresselhaus, 1992]. This in itself might not be a problem if the starting wafer has a higher mobility than the desired mobility. But a major problem with this process for large area devices (which were required for this study) is the appreciable leakage current, which interferes with the measurements. The leakage current can be reduced by depositing a layer of SiO_2 in between the gate metal and the cap GaAs layer, as that reduces the pinhole density. However, since a tunable electron density was not necessary for this study, all devices were made without a gate in order to simplify the processing. For, the final processing parameters, see Appendix B.

4.3) Sample Characterization

Figure 4.4 shows an optical image of one of the samples fabricated using the techniques discussed. Note that the voltage leads are thin and long, and are placed in the center of the Hall bar. The samples were initially characterized in a simple dipstick cryostat. The isolation between parts of 2DEG separated by an etched trench was checked. At room temperature, it was of the order of 10 MΩ in dark, while at 77 K and 4.2 K it exceeded 100 MΩ, the limit on HP34401A digital multimeters. The ohmic contacts were also tested for resistance and linear behavior at 4.2 K.

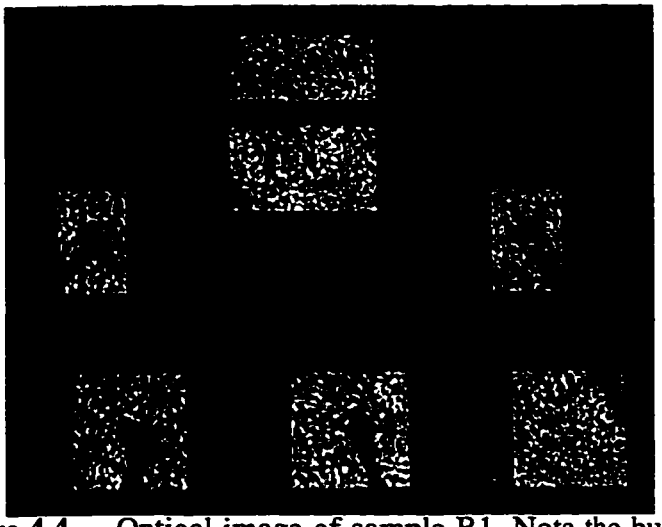

Figure 4.4 Optical image of sample B1. Note the bubbles on the surface of the ohmic contacts (no cap layer). The black long lines at the edges of the image are Au bonds to the sample header.

The electron density was inferred from resistance measurements in the presence of large perpendicular magnetic field. The Landau level quantization produces a longitudinal resistance (R_{xx}) that is periodic in 1/B, known as Shubnikov de-Haas oscillations. The period $\Delta(1/B)$, is related to the electron density by $n_s=2\Delta(1/B)h/e$. Figure 4.5 shows typical data.

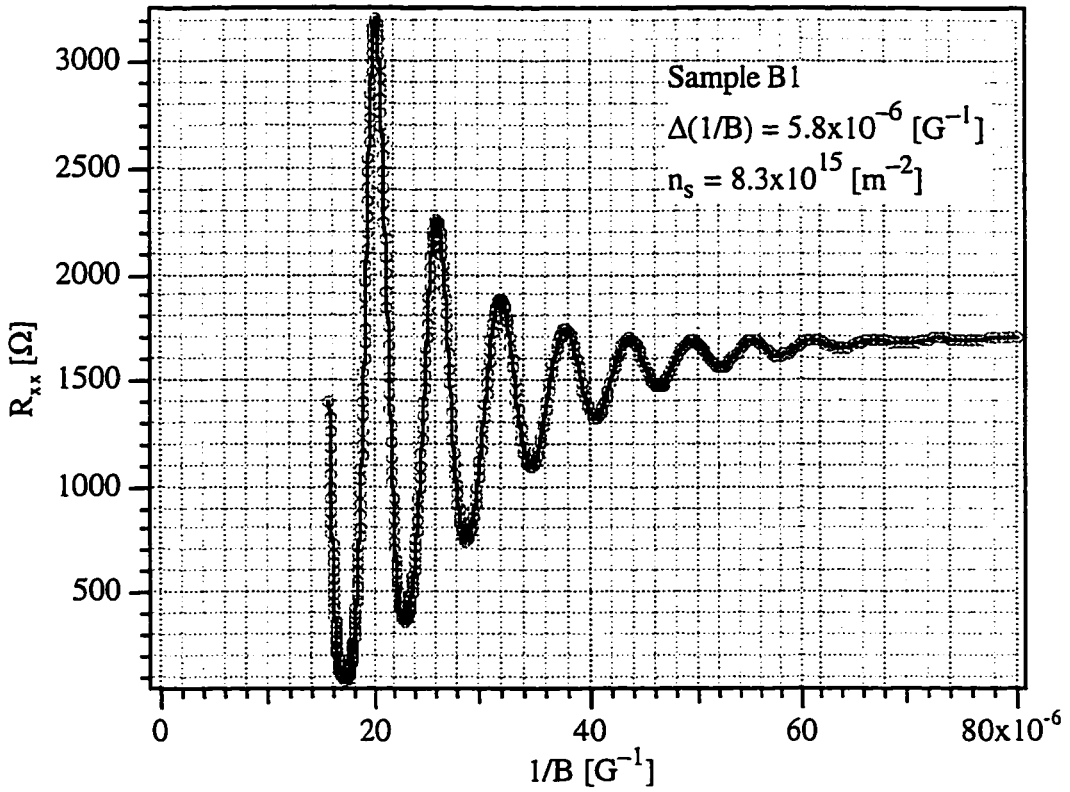

Figure 4.5 Shubnikov-de Haas oscillations for sample B1.

The resistivity, ρ, was obtained using four probe resistance measurements. The low temperature mobility was then calculated using the relation $\mu^{-1}=n_s e\rho$. Table 1 summarizes the parameters of devices, whose results are discussed in this study.

Sample	n_s [10^{15}/m^2]	μ [m^2/Vs]	ρ [Ω]	# of squares	A [10^4 μm^2]
A	1.6	12.4	315	20	20.0
B1	8.3	2.3	327	15	51.7
B2	8.3	2.3	327	15	5.4
B3	8.3	2.3	327	5	51.2
C	2.5	1.4	1786	15	51.7

Table 1. Summary of device parameters. Samples A, B & C are from wafers 748, 903 & G-924 respectively. The sample in Mittal et al., LT-20 paper was also from wafer 748.

Chapter 5

Thermometry

We employ two techniques to determine the electron temperature, T_e. The first method uses weak localization (WL), while the second method uses the sample resistance itself. These give results which are consistent with each other.

5.1) Weak Localization as an Electron Thermometer

In a diffusive system, quantum interference of backscattered electrons along phase coherent paths leads to an increase* in the resistance over the Drude value. Magnetic field reduces the number of such interfering paths, leading to a lowering of this effect. This small increase in resistance at low magnetic fields is what is known as weak localization. The magnetoresistance can be fit to a well established theory of 2D WL [see Appendix C] to find L_ϕ, the phase coherence length. In the absence of other phase breaking mechanisms, a temperature dependence of $L_\phi \propto T_e^{-1/2}$ is expected to hold down to mK temperatures (see Appendix C).

We first measure the magnetoresistance of the sample (Figure 5.1) at a fixed mixing chamber temperature, and extract L_ϕ. Using the same measuring current, we then repeat the measurement at different mixing chamber temperatures from 500 to 40mK. Results for sample A using a measuring current of 14.6nA are shown in Figure 5.2. The straight line is a fit to $L_\phi^{-2} \propto T_{mc}$ for the data points with $T_{mc} \geq 150$mK. Below $T_{mc} = 130$mK, L_ϕ is nearly independent of the mixing chamber temperature. This indicates the electron gas did not reach temperatures below 130mK. We can now use this straight line as an electron thermometer for temperatures above 130mK.

---

* This is true in the absence of spin-orbit (SO) scattering. With strong SO scattering ($L_{SO} \ll L_\phi$) a resistance decrease results.

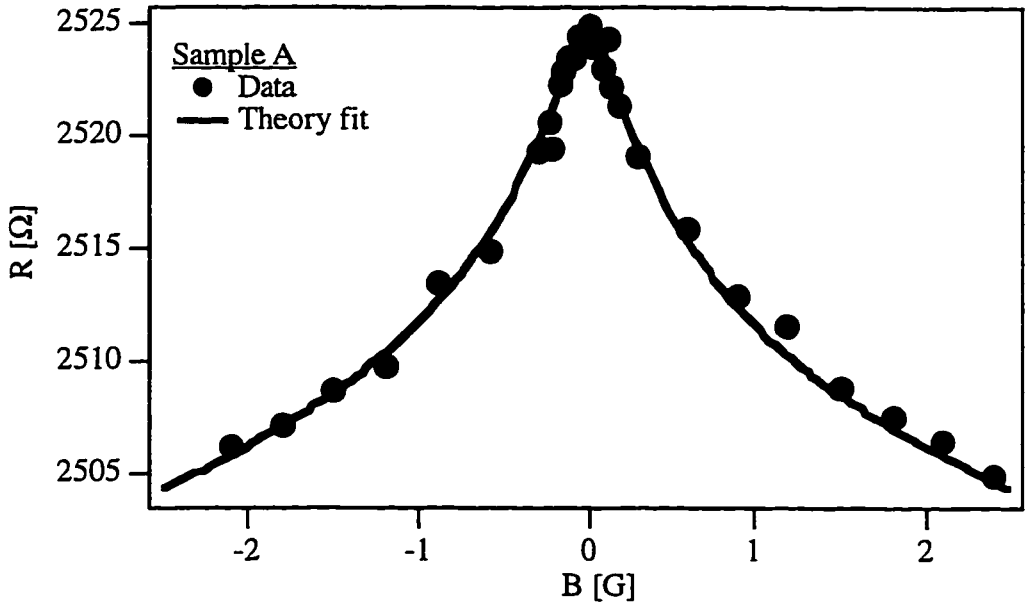

Figure 5.1 Resistance as a function of magnetic field at a fixed mixing chamber temperature. The solid curve is a fit to the 2D theory of Weak Localization, with no adjustable factors.

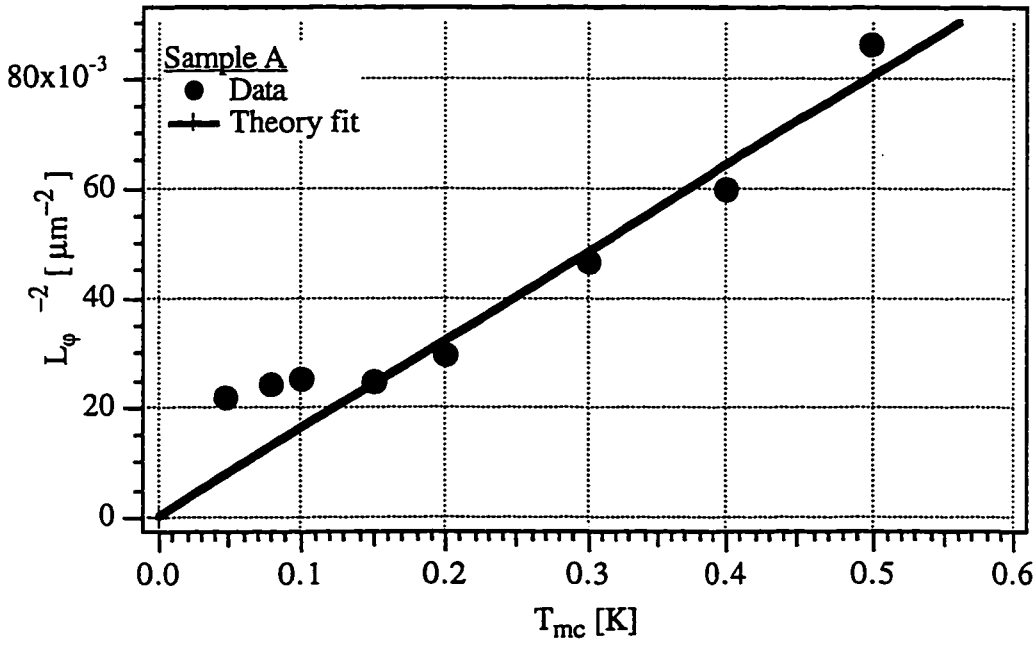

Figure 5.2 Phase coherence length *vs.* mixing chamber temperature. The straight line is a fit to $L_\phi^{-2} \propto T_{mc}$ for the data points with $T_{mc} \geq 150$mK, constrained to go through zero. The slope agrees to the theoretical prediction within a factor of 2 (see Appendix C).

5.2) Sample Resistance as an Electron Thermometer

The second method for determining the electron temperature uses the temperature dependence of the sample resistance, which is primarily due to the electron-electron interaction. This measurement is done at a moderate magnetic field ($B > B_{tr} \equiv h/8\pi el_{tr}^2$), large enough to destroy weak localization (Table 5.1). Figure 5.3 shows the change in the normalized resistance of Sample B1 as a function of the mixing chamber temperature for three different measuring currents 2nA, 20nA and 75nA (the solid lines are an aid to the eye). The curves are identical in the high temperature region, while at lower temperatures the curves for 20nA and 75nA saturate at a lower resistance value. The curve for 2nA was then used to obtain the temperature of the electron gas for the larger current curves, for mixing chamber temperatures greater than 120mK.

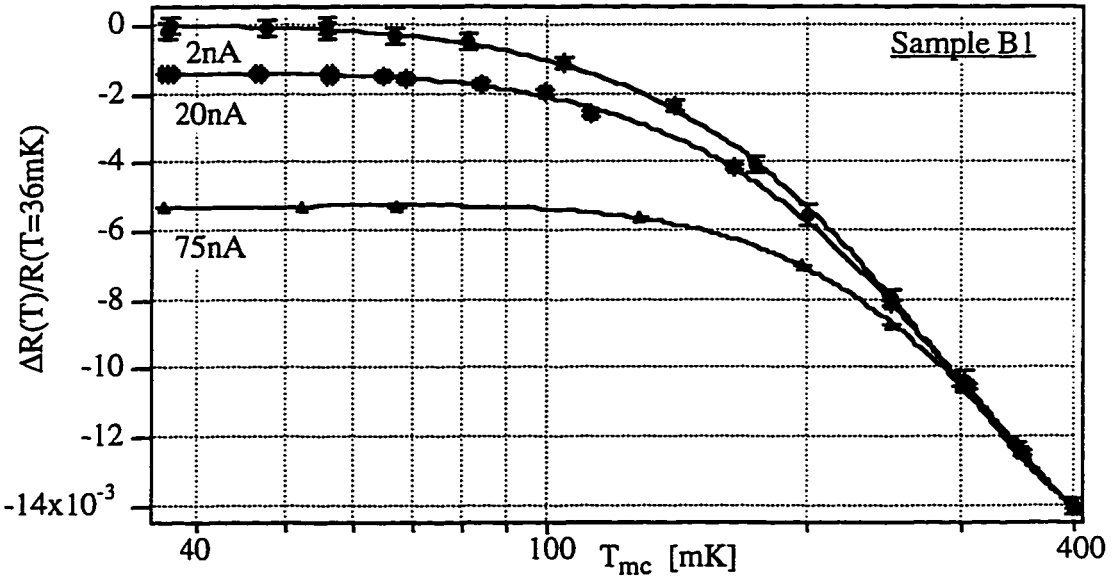

Figure 5.3. Change in the normalized resistance of sample B1 as a function of the mixing chamber temperature, T_{mc}, for different input currents. The solid lines are an aid to the eye. To confirm the stability of our data acquisition setup, measurements were repeated at the lowest and highest T_{mc}. The data was reproducible to within 0.02%.

Sample	B_{expt} [G]	B_{tr} [G]
A	50	2.5
B	250	14.3
C	1500	194.9

Table 5.1 Experimental and transport values of magnetic field at which the sample resistance was used as an electron thermometer.

To confirm that the change in sample resistance is due to electron-electron interactions, it was fit to the theory by Altshuler *et al.* [Altshuler, 1982 in Quantum Theory of Solids]. Figure 5.4 shows a typical fit. The data follow the logarithmic temperature

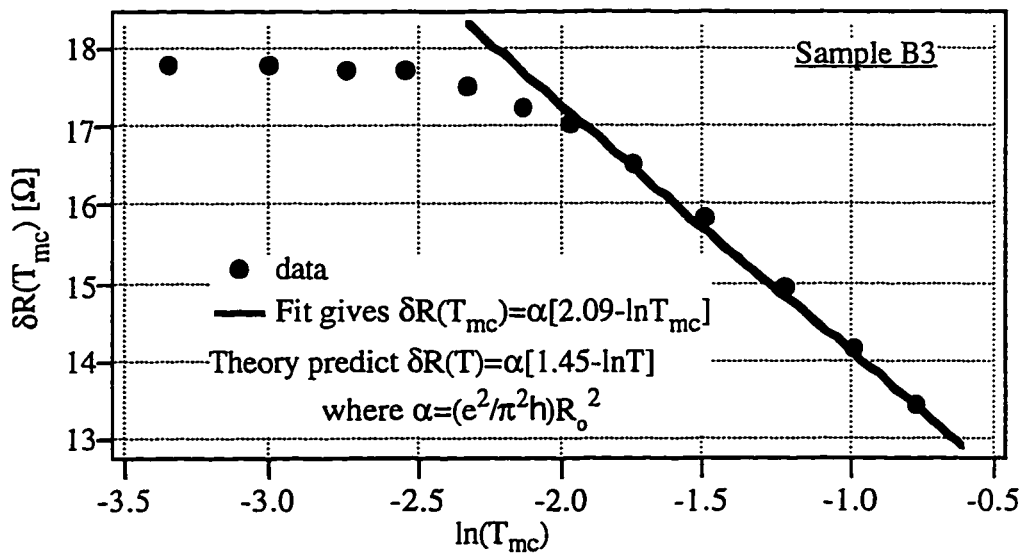

Figure 5.4 Change in sample resistance as a function of mixing chamber temperature and a linear fit to the theory of electron-electron interactions. The fit was done over the high temperature range of the data, and R_o was a free parameter in the fit.

dependence for the change in resistance as predicted with the prefactor α depending on a sample specific resistance R_o. Using R_o as a free parameter in the fit, we get good quantitative agreement too. It is important to realize, though, that the use of the sample resistance as an electron thermometer is not based on the theory of electron-electron interactions. Irrespective of the functional form of the change in resistance with electron

temperature, it can be used as an electron thermometer, as long as it is reproducible and depends only on the electron temperature.

Several groups have used the amplitude dependence of Shubnikov de-Haas oscillations to extract the electron temperature [Karpus, 1988; Hirakawa, 1986; Blyumina, 1986]. This method has two inherent limitations. Firstly, for electron temperatures less than the Dingle temperature (which is essentially a measure of the elastic scattering rate, see Ziman, 1979) this method loses its sensitivity as an electron thermometer. We estimate that even our cleanest sample, A, had a Dingle temperature close to 300mK. Therefore we did not use this approach for measuring the electron temperature in our experiments. Secondly, since the 2DEG resistivity changes substantially as a function of magnetic field, the input power for a fixed current also changes in the same ratio. Thus if the source of heating is a constant current, the electron temperature one extracts would be a function of the magnetic field.

If one uses Shubnikov-de Haas oscillations to measure T_e with the aim of extracting the electron-phonon scattering rate, then the effect of this quantizing magnetic field on the electron-phonon scattering rate should also be considered. None of the groups [e.g., Karpus *et al.*, 1988, Hirakawa *et al.*, 1986, Blyumina *et al.*, 1986] who have used SdH as a thermometer have looked into this issue. Only very recently, it has been proposed [S. Girvin, private communication, 1996, Chow *et al.*, 1996] that the scattering rate would in fact change both in magnitude and its temperature dependence if the magnetic field is sufficiently high and the temperature low enough for the sample to be in the hydrodynamic regime.

Chapter 6

Experimental Apparatus and Techniques

The experiments in this thesis are based on the idea of measuring the temperature of the 2DEG, which is raised above the lattice temperature. This requires first cooling the electrons to the desired temperature, then heating them in a controlled fashion, and lastly measuring their temperature without affecting it. In this chapter, we discuss the experimental set-up and techniques involved.

6.1) Cryogenics

Cooling the 2DEG to mK temperatures first requires a cryostat with the desired base temperature. It then requires good thermal conductance between the cryostat's cold plate and the sample, and finally, minimizing the extraneous sources of power which heat up the electrons above the lattice temperature.

The experiments were conducted in a Kelvinox Dilution refrigerator by Oxford Instruments with a specified base temperature of 30mK. Its mixing chamber temperature was monitored with ruthenium oxide (RuO) thermometers made by Scientific Instruments, which were mounted in a small He filled Cu can with epoxy wire feedthroughs. It was found that a 100 MHz signal from a nearby radio station was heating the RuO thermometer by a few mK above the mixing chamber temperature. This problem was solved by inserting RF filters[1] with a specified attenuation of 46dB at 100MHz into all the leads. In addition, the magnet power supply from Lakeshore produced a large signal around 23kHz, which heated up the RuO sensors from about 30mK to 45mK. This signal was suppressed

[1] The filters were D-type connectors with a pi filter on each lead made by Spectrum Control, Inc. and had a capacitance of 4nF.

with a power filter[2] at the output of the magnet power supply. For details of mixing chamber and sample mount, see Appendix D.

6.2) Sample Mount

The heat flow model we follow assumes the lattice phonons to be at the mixing chamber temperature. To ensure a high thermal conductance between the mixing chamber and the lattice, the sample was Ag painted onto a Jade[3] header whose pins went into an epoxy G-10 socket which in turn was mounted to the mixing chamber with an all Cu path. Thermal conductance calculations [Lounasmaa, 1988] for this heat flow path predict the lattice temperature to be within few μK of the mixing chamber temperature for a maximum heat load of 1pW. We have confirmed this experimentally by mounting a RuO sensor from the same production batch as that for the mixing chamber in an identical fashion near the sample to measure the lattice temperature. The two sensors tracked each other to within 3-4mK at the lowest temperatures, close to the interchangibility claimed by Scientific Instruments.

At mK temperatures, power levels as small as 1pW can raise the temperature of the 2DEG electrons above that of the lattice phonons. Therefore having the GaAs lattice at the mK mixing chamber temperature does not necessarily imply that the 2DEG is at that temperature as well. The 2DEG is thermally anchored to the mixing chamber through the ohmic contacts, the wire bonds, the header and the socket pins, and the measurement leads attached to the sockets. The leads were made of 30 A.W.G. copper, and were tightly wrapped several times around a copper post attached to the mixing chamber, which itself was made of copper. The sockets pins and the wire bonds were made of Au. We did not

[2]The power filter was Filter Concepts model LE100LH (100 A, 250 VAC).
[3]Custom designed by Jade Corp., Pittsburgh, PA.

use Al bonds to avoid a section of superconducting material in the thermal path. This ensured that the ohmic contacts were within 1μK of the mixing chamber temperature. We took great care to fabricate ohmic contacts with low electrical resistance for high thermal conductance via electron diffusion. The only shortcoming of the above scheme resulted from the SnPb solder joints between the leads and the socket which turns superconducting below 5K. Experimentally, however, this was not a problem since most measurements were conducted at magnetic fields above the critical field of the solder.

6.3) Extraneous Sources of Power

In order to raise the temperature of the electron gas in a controlled fashion, the power which heats them up should be known precisely. Any extraneous sources of power should be made smaller than the input power levels. These extraneous sources broadly fall into two categories.

The first is blackbody radiation which heats up the sample surface, and then couples to the electrons via phonons in the lattice. The sample is surrounded by a vacuum can maintained at 4.2K. For typical sample geometries, the incident radiation is of the order of few pW. Even if all of this is absorbed by the phonons, the electron temperature would rise by only a few μK. In one of the experiments, the temperature of the vacuum can was reduced to 2K by pumping on the refridgerator lambda coil. No measurable change was seen for the the mixing chamber or the sample temperature. This confirms that blackbody radiation was not the dominant extraneous source of power.

The second source of extraneous power is electromagnetic pickup, which couples to the electron gas through the measuring leads. It is generally the limiting factor in cooling the electrons. High frequency pickup at frequencies above 10kHz from sources such as radio station, computer screens etc. can be reduced by low-pass filtering. All signals lines were filtered with a commercial pi filter with a specified cutoff frequency of 800kHz at the

feedthrough into the cryostat, and with a 1nF capacitor to ground at the mixing chamber. It was not possible to use larger capacitors for even lower cutoff frequencies because the resulting phase shifts would interfere with the lock-in measurements. For details of shielding and filtering of sample leads, see Appendix D. The above scheme reduced the power levels from about 0.5pW to less than 0.01pW.

6.4) Measurement Setup

With the dilution refrigerator reliably attaining base temperatures of 30mK and with the sources of extraneous power coupling into the 2DEG suppressed below 10fW, we were in a position to perform the desired experiments. We used Joule heating to raise the temperature of the electron gas above the lattice temperature, and measured its temperature using either sample resistance or weak localization techniques as discussed in Chapter 5. Both techniques were essentially resistance measurements, either at a fixed magnetic field or as a function of field. They were done using standard four probe low frequency techniques with lock-in amplifiers (LIAs) . We used Princeton Applied Research (PAR) lock-in amplifier models 124 or 126 with PAR 116 or 117 differential preamplifiers at a frequency of 13 or 17 Hz. AC measuring current was used both for heating and thermometry purposes.

We have done calculations to confirm that low frequency AC and DC currents yield nearly the same results for heating when the dominant mechanism for heat flow is phonon emission. If the same average power flows for both the AC and DC cases (i.e. $|I_{ac}|=\sqrt{2}I_{dc}$) and $T_e \gg T_{ph}$, then we predict the measured voltage signal at the first harmonic of the lock-in to be 7% larger for AC heating as compared to DC heating[4]. Our mesurements of heat flow as a function of electron temperature (see Chapter 7) yield the same power laws after

[4]On the other hand, if electron diffusion is the dominant mechanism for heat flow and $T_e \gg T_{ph}$, then the measured signal is about 20% larger for AC heating as compared to DC heating.

including this correction. Therefore, none of the data or the results shown here have been compensated for this effect.

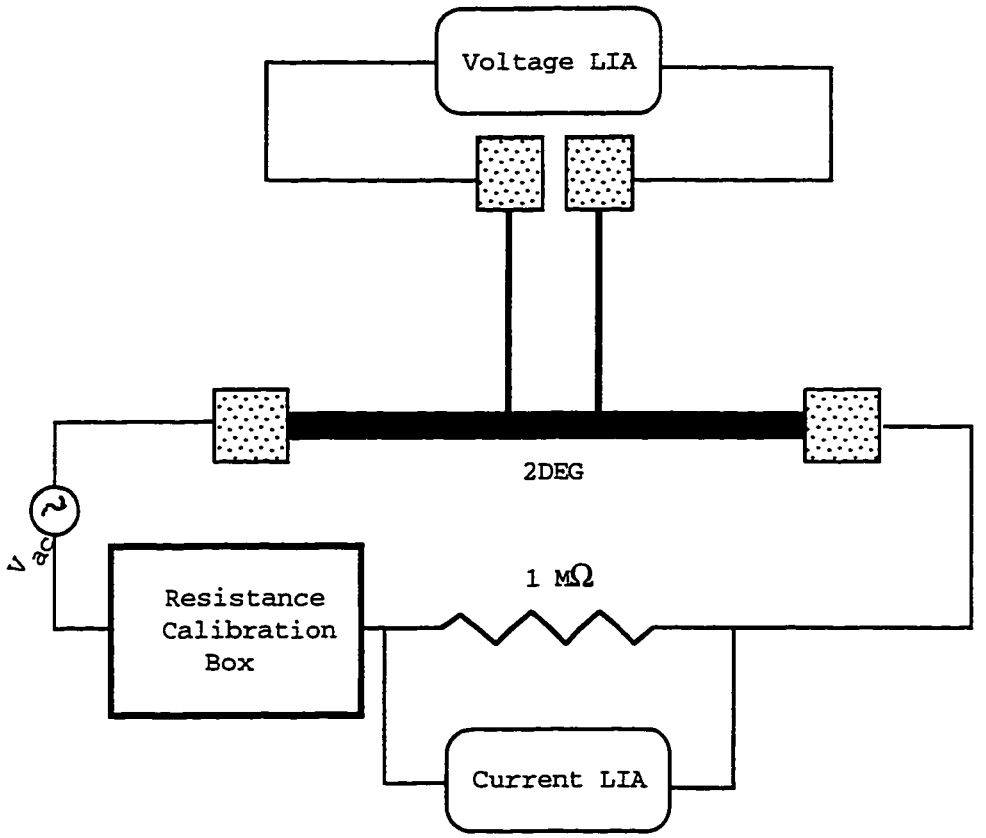

Figure 6.1. Circuit for resistance measurements. The dotted boxes represent the ohmic contacts.

Figure 6.1 shows the circuit representation of the set up used. The AC voltage signal was taken from HP239A oscillator, which had a more stable frequency (± 3% of selected range) compared to the LIA in-built source, and had less noise associated with it. It was converted to a current source with a 1MΩ resistor in series with the sample and the calibrating resistors. One LIA was used to measure the current by sensing the voltage across the 1MΩ resistor, and another measured the voltage across the device. Up to three devices were measured in series to save time and liquid He, and to ensure identical measurement conditions when comparing different devices.

The output of each LIA was measured with a digital voltmeter with a GPIB interface (HP3478A) and the data were recorded by a Macintosh IIci computer using LabView software from National Instruments. A library of LabView virtual instruments and data acquistion routines was created for obtaining automated traces of resistance as a function of time or magnetic field. For fixed magnetic field studies and the Shubnikov-de Haas measurements, the superconducting magnet was controlled by Lakeshore Cryotonics Model 612 Magnet Power Supply. This unipolar power supply provided current steps of 1mA, which translates into field steps of 1.066G. The weak localization measurement required step sizes of the order of mG, and a bipolar magnetic field. For these purposes, a HP Harrison 6823A bipolar DC power supply was used along with a Yale built magnet shunt box. The voltage of this power supply was controlled at its output by HP59501B digital to analog power controller, which was in turn controlled by the computer.

The LIAs were calibrated using a home built calibration resistor box with resistance values ranging from 1Ω to 11kΩ. Readings were taken at two known resistance values spanning the expected range of device resistance to find the multiplicative factor and the offset needed to convert a measurement of the LIA voltage to an accurate resistance. It was important to have the calibration resistor box in series with the sample rather than replacing the sample by a resistor for calibration purposes in order to ensure identical phase[5] shifts during the actual measurement and the calibration procedure. Whenever any of the LIA settings or the input current was changed, the calibration was repeated. The stability of the calibration was also confirmed over a time period[6] involving a complete R *vs.* T_{mc} or weak localization measurement.

---

[5]The phase of the voltage LIA was set to zero while measuring the calibration resistors. It was then not adjusted when the sample resistance was measured. This is an accurate technique provided $(\omega RC)^2 << 1$, where C is the effective capacitance across the sample resistance, R. In our experiments, ωRC was typically of order 10^{-4}.

[6]This was up to 8 hours for a measuring current of 1nA when the preamplifier MN2311 wasn't used.

In order to characterize the accuracy of our setup for resistance measurements, we used the phenomenon of Landau quantization (see Beenaker and van Houten, 1991 for a review). In the presence of large perpendicular magnetic field, the transverse sample resistance (ρ_{xy}) is quantized in steps of $(h/e^2)/2n$, where n denotes the Landau level. As can be seen from Figure 6.2, the resistance measurements were accurate to 2 parts in 10^4.

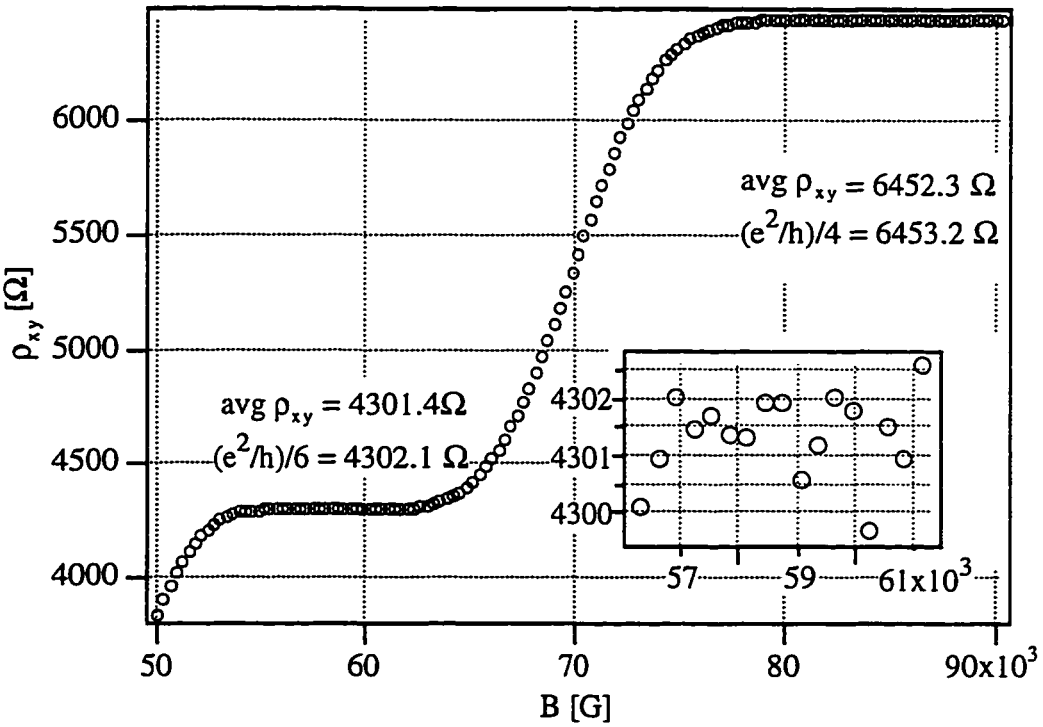

Figure 6.2 Transverse resistance for magnetic fields corresponding to Landau levels n=3 and n=2. The average values on the plateaus (4301.4 Ω and 6452.3 Ω) agree with the $(h/e^2)/6$ and $(h/e^2)/4$ to within 0.02%. Inset shows the n=3 Landau level in greater detail.

Current levels as low as 1nA were used for measuring typical sample resistances of order 1kΩ. For a desired accuracy (see e.g., Figure 4.3) of a few parts in 10^4, voltage levels of less than 1nV had to be accurately detected over the duration of the measurement.

In order to achieve this goal, the performance of the LIAs used was carefully characterized. In particular, drift in the gain was carefully recorded as a function of laboratory temperature, humidity and power supply fluctuations over time periods. It was

found that typical drifts ranged from 100-1000 ppm in a time period of 8-10 hours for different LIAs. For all the LIAs, the drifts were independent of frequency and roughly of the same magnitude as percentage of the signal on all scales. In the presence of so many uncontrolled variables, no definite conclusions could be drawn as to the source of the drift, but we suspect it to be related to temperature drifts[7]. Effort was then directed towards minimizing the noise level in the set up in order to reduce the total measurement time and hence the LIA gain stability requirements.

To reduce the pickup noise great care was taken to avoid ground loops. Tightly twisted coaxial cables were used to reduce the effects of magnetic pickup and watertight metallic enclosures were used to prevent high frequency pickup. After these changes in the set up, the noise was limited by the input noise of the PAR preamplifiers, which is about 8-10nV/$\sqrt{Hz}$. This was further reduced by using a higher LIA time constant (typically $\approx$ 3s) and averaging more readings (typically 3-10). But in order to avoid long and costly measurements, a preamplifier with a lower input noise was built.

MN2311 instrumentation amplifiers from Micro Networks[8] were used as low frequency voltage preamplifiers. They were built into small stand-alone units whose output BNCs were connected directly to the input BNCs of the PAR preamplifier. They were powered by four 6V lithium batteries in series with a combined capacity of 5200 mAh for continuos use over 200 hours without drop in supply voltage. The preamplifiers were used with a double ended output to utilize the high CMRR of the PAR preamplifiers, and had a fixed and stable gain of 200. The instrumentation amplifiers had a JFET input stage with extremely low noise characteristics. Figure 6.3 shows their voltage noise measured with the inputs shorted to ground. The noise was found to be white and around

[7]LIA 124 which had the best observed behavior, has an instrument specification of 200 ppm/°C as the typical value for drift in gain with temperature. Considering the lack of temperature control in the laboratory, even opening and closing the laboratory door could lead to the observed drift.
[8]Micro Networks, Worcester, MA 01606.

1.9 nV/√Hz with a 1/f knee below 6Hz. The specified current noise of 4 fA/√Hz could be neglected since sample resistances were always below 15 kΩ. Reducing the noise by a factor of 4 compared to the PAR preamplifiers allowed us to speed up the data acquisition by a factor of 16, thereby reducing the requirements on the stability of lock-in amplifiers and saving the cost of LHe.

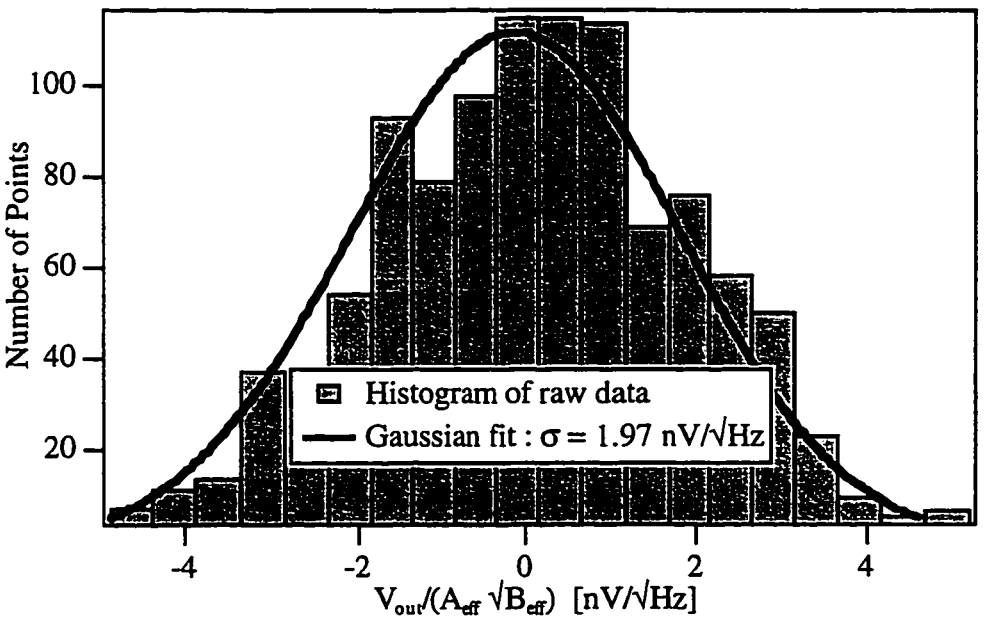

Figure 6.3 Gaussian fit to the measured noise of MN2311 preamplifier with inputs shorted to ground, and the outputs into the PAR preamplifier of LIA 124. The noise measured at the LIA output has been converted into the input noise at MN2311 inputs by dividing with the effective gain and square root of effective bandwidth for the setup.

Chapter 7

Results and Analysis

7.1 Heat Flow measurements

Using Joule heating from the measuring current we dissipate a known amount of power in the 2DEG such that phonon emission is the dominant energy relaxation mechanism. We then determine the electron temperature. The power levels used exceed any extraneous power dissipated in the device. Figure 7.1 shows the results for sample A. It also shows the theoretically predicted total power flowing out of the 2DEG, using the Price prediction (eq. 3.1) for the phonon emission contribution. The experimental data are in agreement with the theory, showing the first experimental verification of Price theory.

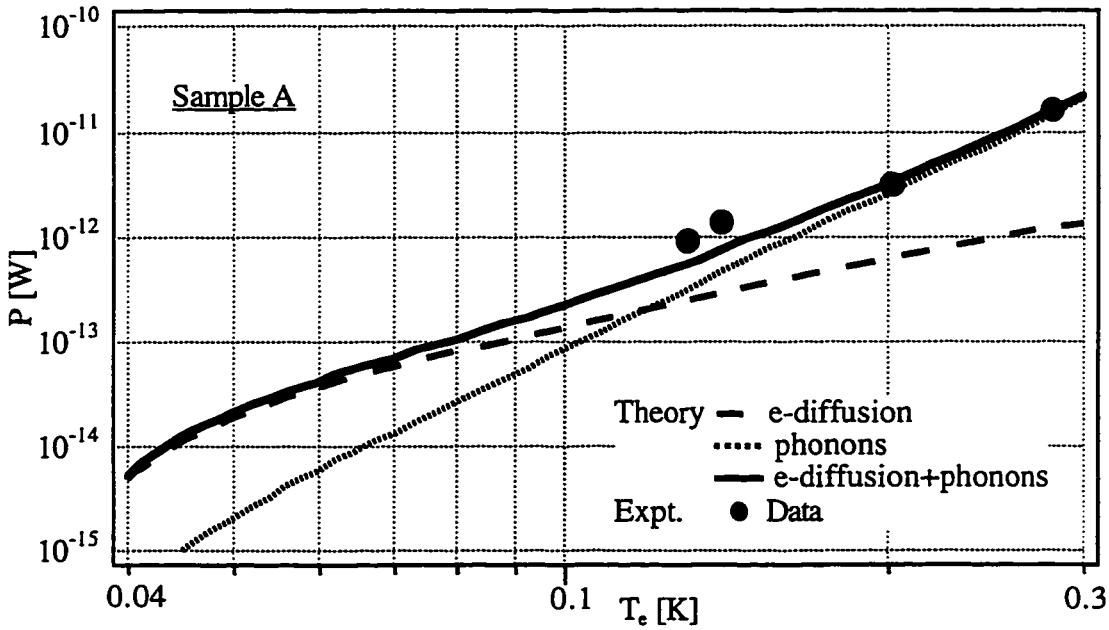

Figure 7.1 The power flowing out of the 2DEG as a function of the electron temperature at T_{ph} = 36mK for sample A. The dotted curve for the phonons is the Price prediction.

In order to understand the role of disorder, we then measured sample B1, which had a lower mean free path as compared to sample A (see Table 7.1). It was designed to have the

same number of squares and a sheet resistance close to that of sample A (see Table 4.1) ensuring that the thermal conductance due to electron diffusion is similar for the two devices. The results are shown in Figure 7.2. The dotted line representing the heat flow due to phonon emission follows the functional form $P_{e\text{-}ph} = \alpha(T_e^5 - T_{mc}^5)$ (eq. 2.1 with p=5). The value of α is chosen such that when added to the electron diffusion contribution (dashed line), it fits the experimental data best. For this more disordered sample, the heat flowing out via phonon emission still shows a temperature dependence proportional to T_e^5 which is dictated by phase space arguments, but its magnitude exceeds the value predicted by Price for the clean limit. All fits to P *vs.* Te data discussed in this chapter (except for the clean sample A) therefore consider α (which is proportional to the magnitude of the phonon contribution to the heat flow) as a free parameter in the fit.

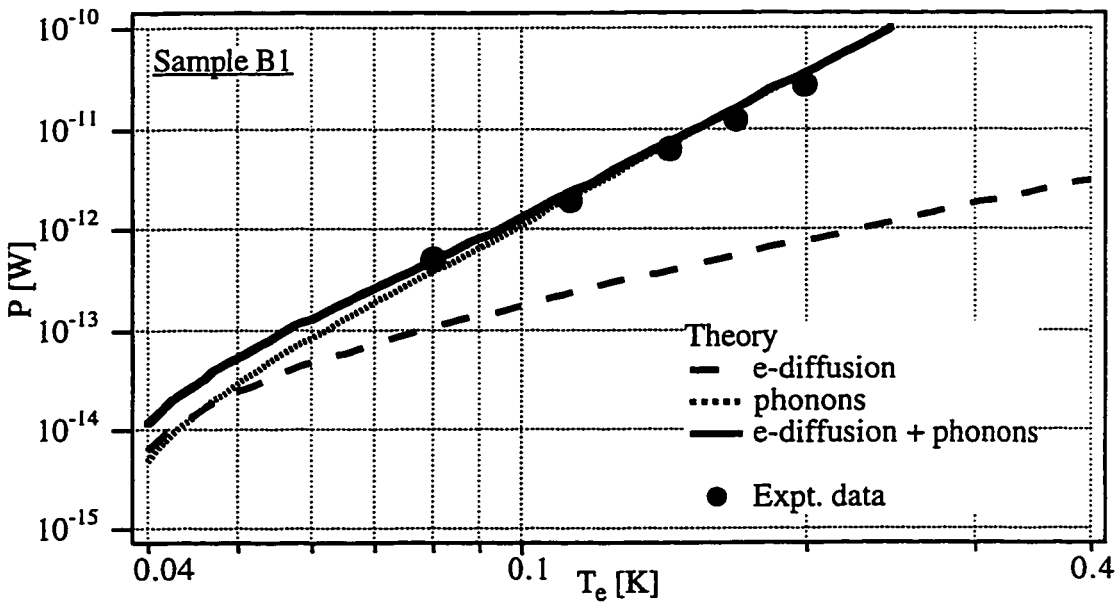

Figure 7.2 The power flowing out of the 2DEG as a function of the electron temperature at T_{ph} = 36mK for sample B1.

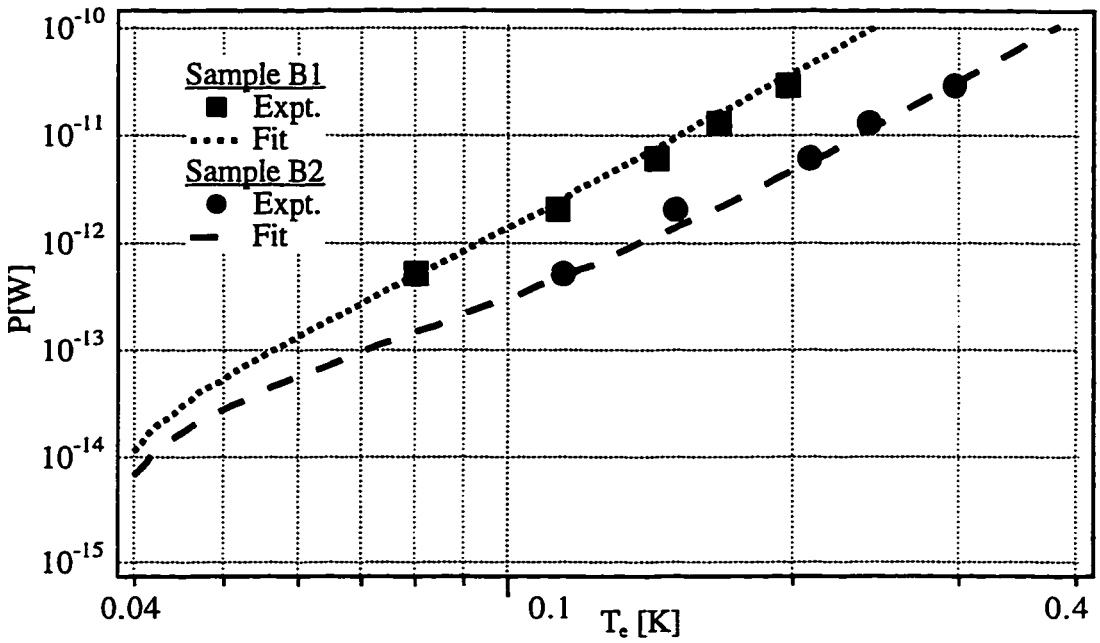

Figure 7.3 The power flowing out of the 2DEG as a function of the electron temperature at T_{ph} = 36mK for samples B1 and B2 measured in series.

In order to confirm that the observed heat flow was indeed due to phonon emission, we measured samples B1, B2 and B3. They were on the same chip, and were measured in series two at a time[1], ensuring a comparison based solely on the geometrical differences between them. We first measured B1 and B2 which had the same number of squares, and hence an identical thermal conductance due to electron diffusion, but B1 had an area about nine times larger than B2. Figure 7.3 shows the data and the fits, with the fit being done using the *same value of* α. As can be seen, the heat flowing out of the two devices scales with the device area. This confirms that the dominant mechanism for energy relaxation is phonon emission.

[1] They could not be measured all at the same time because of lack of enough lock-in amplifiers and digital multimeters.

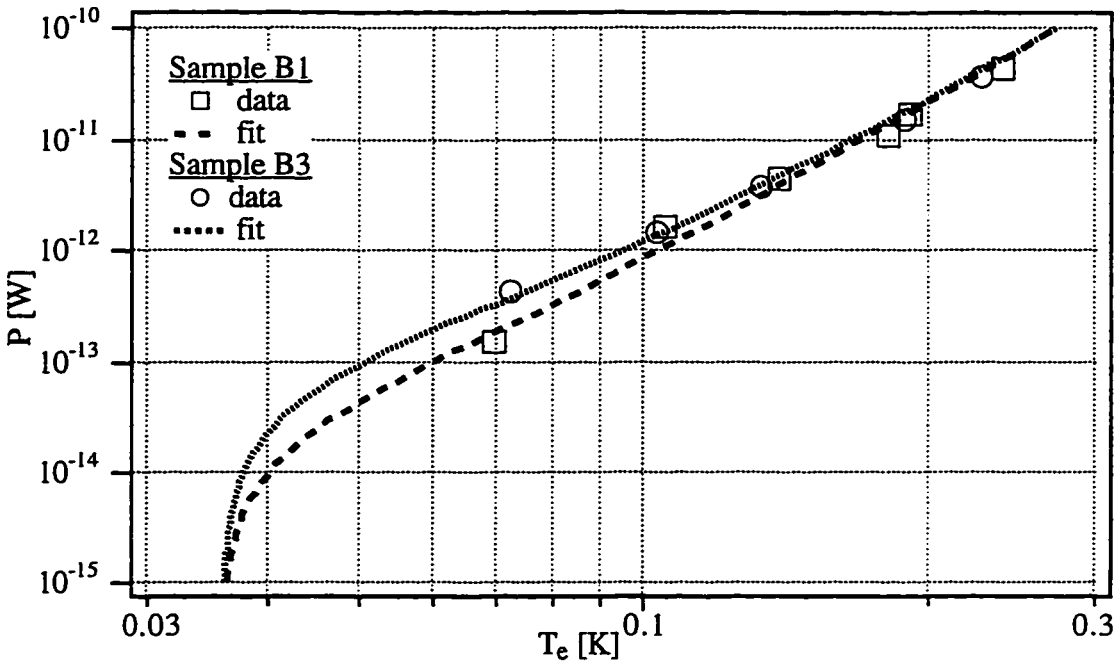

Figure 7.4 The power flowing out of the 2DEG as a function of the electron temperature at T_{ph} = 36mK for samples B1 & B3 measured in series.

We repeated the experiment after thermally cycling the devices to room temperature. This time we measured samples B1 and B3, which had different number of squares, but the same area. Figure 7.4 shows the results. Again, the lines represent fits to the data with the fit being done using the *same value of* α. We can see that the same heat flows out in both the devices down to about 100mK. This confirms that even though the magnitude of heat flow exceeded the value predicted by Price, the operating mechanism was energy relaxation due to phonon emission.

Note that below about 100mK, we start seeing heat flow due to electron diffusion. Sample B1 is hotter than sample B3 for the same heat flowing out of the two devices. This is consistent with heat flow due to electron diffusion as B1 has more number of squares than B3, and hence a larger Wiedemann-Franz thermal resistance.

The existing theories [Price,1982; Karpus, 1988] for heat flow by phonon emission are valid if the electrons only occupy the first subband in the GaAs/AlGaAs

heterostructure. As mentioned in Chapter 2, some groups [Kreschuk *et al.*, 1988; Ma *et al.*, 1991] have seen an increase in the power flowing out via phonon emission due to intersubband scattering. This happens if the density is high enough that the second subband is also populated. Using Shubnikov-de Haas measurements we confirmed for all our samples that only the first subband is occupied. Figure 7.5 shows the Fourier transform of R(1/B) of typical Shubnikov-de Haas oscillations for the sample with the highest density. Clearly, there is only one peak in the Fourier transform confirming that only one subband is occupied. Moreover, previous work [Klepper, 1991] showed that the second subband occupation for the heterostructures used does not occur even at a density of $8.8 \times 10^{15}/m^2$, which is higher than $8.3 \times 10^{15}/m^2$, the measured density for Samples B. Thus, we believe that the increased heat flow for our Samples B is not due to intersubband scattering, but due to disorder.

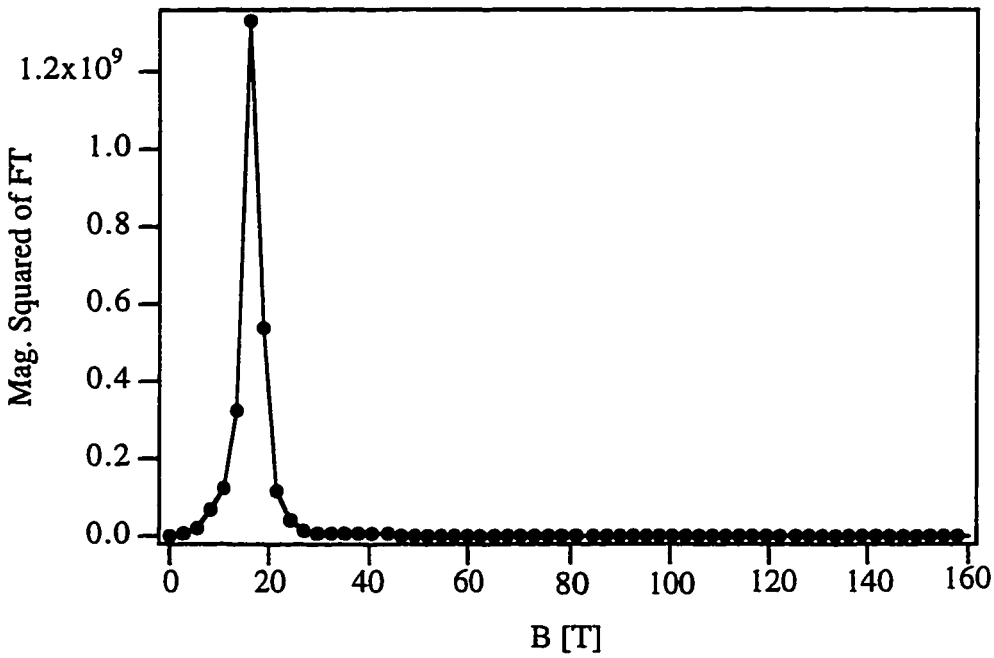

Figure 7.5 The magnitude squared of Fourier transform of Shubnikov-de Haas oscillations shown in Figure 4.4. The single peak indicates a single period in the oscillations of R *vs.* 1/B.

In order to further investigate the disorder dependence, we measured sample C which had a mean free path much smaller than the samples A and B (Table 7.1). It also had a

density low enough that second subband occupation would not be an issue at all. The results are shown in Figure 7.6. The solid line depicts the fit to the data as discussed earlier. As with samples B, the magnitude of the power flow exceeds the predicted value for the clean limit, and still shows a temperature dependence proportionally to T_e^5.

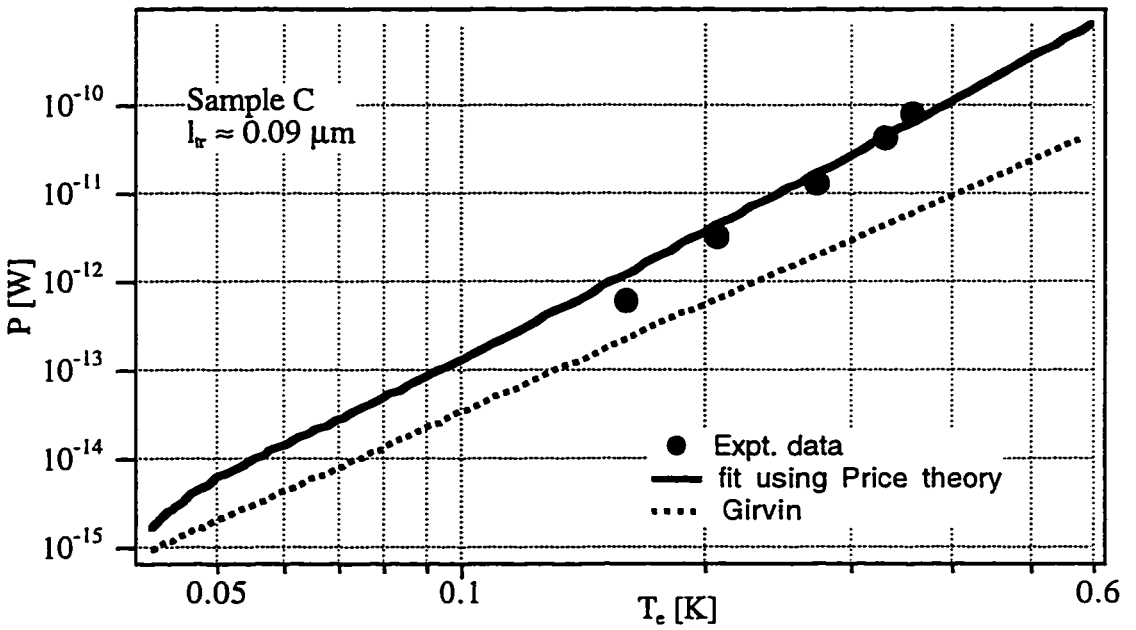

Figure 7.6 The total power flowing out of the electron gas as a function of its peak electron temperature for sample C. The solid line is a fit to the data using scaled Price theory, which has a temperature dependence of T_e^5. The dashed line shows Girvin's prediction, which follows T_e^4.

As discussed in Chapter 3, very recently Girvin *et al.* [Girvin, S., private communication; Chow *et al.*, submitted to PRL, 1996] have put forward a theory which considers the effects of disorder on the heat flow due to phonon emission. They predict that in the hydrodynamic regime, the temperature dependence of the power flowing out changes from T_e^5 to T_e^4. In the hydrodynamic limit, momentum conservation is lost because of frequent collisions with the impurities. The rate at which the energy is absorbed by the 2DEG from a phonon mode is independent of phonon wave vector and frequency. Hence the 2DEG acts like a black body and emits phonons with a T^4 spectrum.

The transition to this hydrodynamic regime takes place when $ql_{tr} << 1$. As can be seen from Table 7.1, none of our samples satisfy this criterion over the measurement regime except maybe the lowest temperature data point[2] for sample C. Figure 7.6 shows the heat flowing out for Sample C based on Girvin's theory. Clearly our data do not agree with his theory either in magnitude or in the temperature dependence. The fact that the lowest temperature data point does not fall on the fit to the functional form $P_{e\text{-}ph} = \alpha(T_e^5 - T_{mc}^5)$ may not be significant. We do not think that we are seeing any signatures of transition to the "hydrodynamic" regime.

Sample	l_{tr} [μm]	ql_{tr} @ 0.1K	ql_{tr} @ 0.5K
A	0.82	4.53	22.65
B	0.34	1.88	9.38
C	0.09	0.52	2.63

Table 7.1 Transport mean free path and ql_{tr}

7.2) Electron-Phonon Scattering Rates

Having measured the power flowing out of the 2DEG due to phonon emission, we can now extract the electron-phonon scattering rate as a function of the electron temperature. Using eqs. 2.1 and 2.2, we get

$$\tau_{e-ph}^{-1} = \left(\frac{5}{A\gamma}\right)\left(\frac{P_{e-ph}}{T_e^5 - T_{mc}^5}\right)T_e^3. \qquad (7.1)$$

This equation can be used to extract $\tau_{e\text{-}ph}^{-1}$ for each P *vs.* T_e data point. Further plotting the electron phonon scattering rate as a function of T_e^3, we can extract an average scattering rate from the slope of the linear fit, which is constrained to go through zero. Figure 7.7 shows the results for sample B1. As can be seen, the electron-phonon scattering rate is proportional to T_e^3, and is about 1GHz at 1K.

[2]It is debatable whether this data point belongs in the hydrodynamic regime. According to Prof. Girvin, ql_{tr} should be less than 1/3 for the sample to be strictly in the hydrodynamic regime, although there is no theoretical proof for this factor of 1/3.

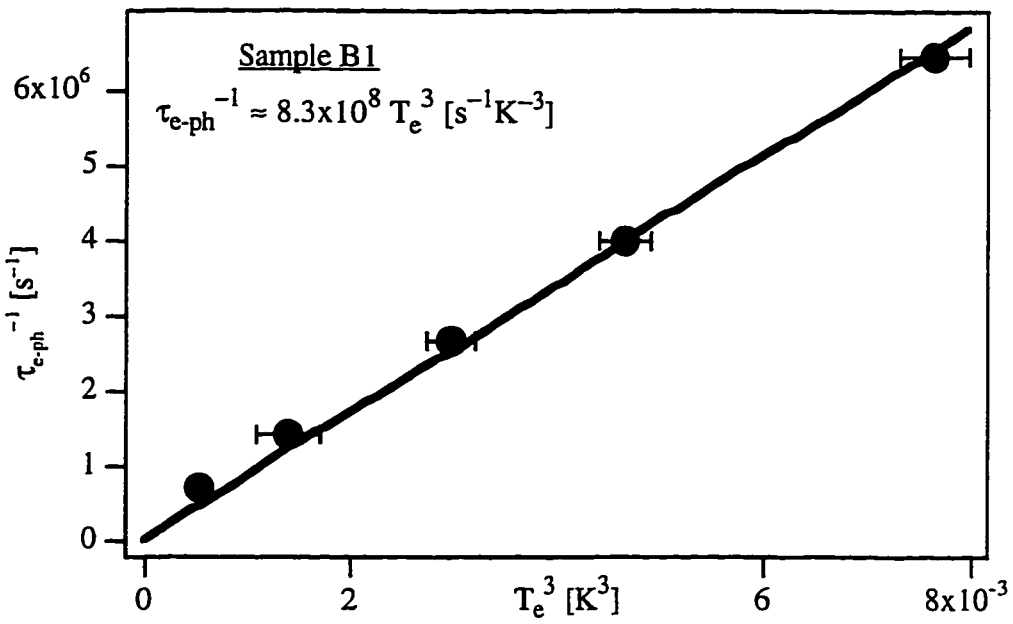

Figure 7.7 The electron-phonon scattering rate as a function of electron temperature for sample B1. The straight line is a fit constrained to go through zero.

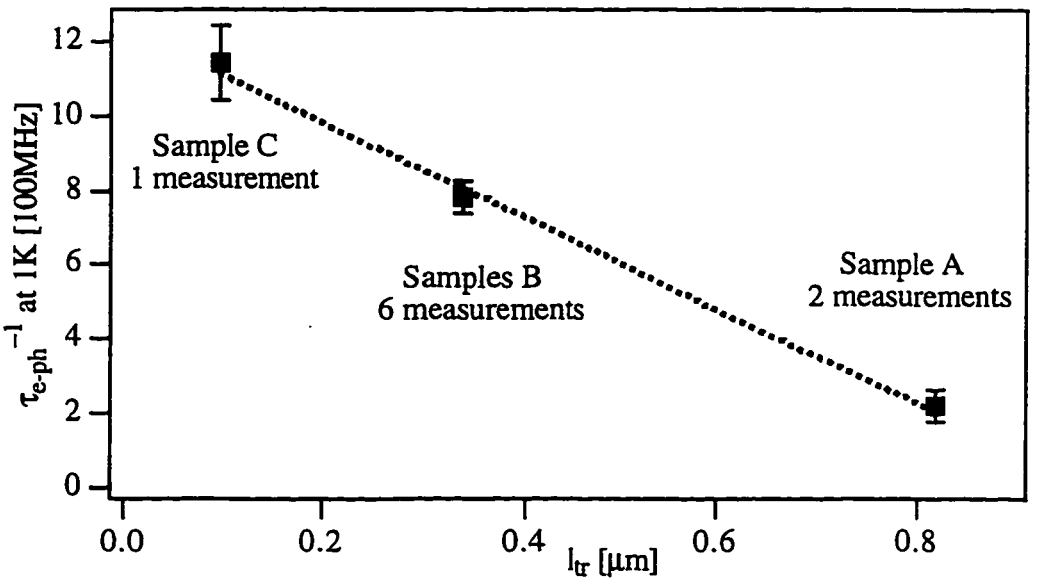

Figure 7.8 Electron-phonon scattering rate as a function of the transport mean free path.

Performing a similar analysis for all our measurements, we plot the measured electron-phonon scattering rates as a function of the transport mean free path. As can be

seen from Figure 7.8, the electron-phonon scattering rate increases with decreasing mean free path over nearly one decade of variation in the mean free path. As discussed before, sample C maybe just enters the hydrodynamic regime, while sample A agrees with the theoretical prediction in the clean limit. Thus, in our experiments,we have measured the electron-phonon scattering rate from the clean to the very dirty limit. Theories for electron-phonon scattering rate exist in both these limits but not in between.

We can now try to understand the role of disorder in this regime between the two extreme limits. Consider an electron-phonon scattering event in which an electron in a state $\hbar k_1$ emits a phonon with wave vector q. The final k state of the electron is fixed by momentum conservation to be $\hbar k_2 = \hbar k_1 - \hbar q$. But this momentum conservation holds only to within Heisenberg's uncertainty principle. The electron momentum in a disordered system is uncertain by an amount of order $\hbar/l_{tr}$. Thus, a smaller l_{tr} leads to an increased phase space for the scattered states and hence a higher scattering rate. In the clean limit, l_{tr} is large and hence the increase in the scattered phase space is small. In the dirty limit, momentum conservation does not hold, and the above argument does not apply. Our data which lies in between the clean and dirty limit, does follow the trend of increasing electron-phonon scattering rate with decreasing mean free path. However, a precise theory addressing the issue of dependence of the electron-phonon scattering on disorder in between the clean and dirty limits is yet to be formulated. It would also be desirable to measure the scattering rate in samples cleaner than sample A and dirtier than sample C in order to touch the true clean and dirty limits respectively.

Chapter 8

Conclusions

We have measured the heat flow out of a GaAs 2DEG below 0.5K. We find that the heat flowing out due to phonon emission has a temperature dependence proportional to T_e^5 as dictated by phase space arguments and predicted by Price. The measurements for the cleanest sample agree quantitatively with this prediction. This constitutes the first experimental verification of the Price theory in the screened Bloch-Grüneisen regime.

We have extracted the electron-phonon scattering rate, and find a temperature dependence proportional to T_e^3 for all our samples, and a magnitude of $2x10^8$ s^{-1} at 1K for the cleanest sample. We have measured several samples which span the range of disorder from the clean to almost the dirty limit. The electron-phonon scattering rate is found to increase with decreasing mean free path over nearly one decade of variation in mean free path. These are the first measurements of the electron-phonon scattering rate as a function of the mean free path in a GaAs/AlGaAs 2DEG. Theories have only been formulated for the very clean [Price, 1982] and dirty [Girvin, 1996] limits. Our measurements bridge the gap, and should stimulate theoretical work in this regime.

In the future, to completely understand the disorder dependence of the electron-phonon scattering rate, it would be desirable to measure it in a sample whose mean free path is systematically varied from the very clean to the very dirty limit. In fact, starting from a high mobility sample, one can degrade its mobility in small steps using reactive ion etching, and measure the scattering rate as a function of the transport mean free path in the *same* sample.

Our study has important general implications for low temperature experiments. Since electrons are thermally decoupled from the phonons at mK temperatures even with heat

loads less than 1 pW, it is essential to differentiate between the electron temperature and the bath temperature. This is especially true for studies which involve measuring a temperature dependent property of the electronic system, or which critically depend on the system attaining a desired low temperature. Also, certain low temperature applications require the heat to flow out either by phonon emission or by electron diffusion [e.g., see Prober, 1993]. This study gives an insight into controlling the heat flow mechanisms and achieving a desired electron temperature by careful sample design.

This study was focused on measurements of the electron-phonon scattering rate, and hence the samples were designed such that in the temperature regime of interest, phonon emission was the dominant mechanism for heat flow. We see that the heat flow by phonon emission scales directly with the area of the 2DEG, and we have therefore designed samples with large area such that phonon emission is the dominant mechanism for heat flow even at mK temperatures. One should also keep in mind that a more disordered sample will achieve a lower temperature as long as phonon emission dominates. On the other hand, if heat is flowing out by electron diffusion, then a less disordered sample will achieve a lower temperature. We also see signatures of heat flow being affected by electron diffusion at the lowest temperatures (Figure 7.4). In future studies, heat flow due to electron diffusion can be measured using devices with low electrical resistivity and small lengths.

The unique dimensionality offered by the 2D electron gas made it easier to separate and control the phonon emission contribution to heat flow from that due to electron diffusion. The three-dimensional nature of the phonons in a GaAs/AlGaAs heterostructure allowed us to study just the disorder dependence of energy relaxation rate for 2D electrons without phonon dimensionality being an issue. And surprisingly, unlike electrical conductivity which decreases with increasing disorder, the thermal conductivity was found to increase with increasing disorder.

Appendix A

Numerical Simulation of Temperature Profile

The following program, written in FORTRAN calculates the temperature profile along the length of the Hall bar when heat flows out by electron-diffusion, phonon emission or both mechanisms. It is based on eq. 3.19 discussed in the text. The strength of the phonon or electron diffusion contributions can be adjusted as desired.

The temperature is calculated as function of input current for a fixed set of sample parameters. The program takes in various input parameters such as the minimum and maximum value of the current, the number of current steps, the device length and width, sheet resistance, electron density, the phonon temperature and the ohmic contact temperature, and outputs the temperature of the electrons along the length of the Hall bar. It also outputs the temperature in the center of the Hall bar as a function of the input power.

```
c  Program Main
c  Give imax as an odd number
   parameter (imax=51)
   common/temp/t(imax),x(imax),tsq(imax)
   real length,ns,lorentz
c*************************************************************
   open(unit=1,file='pvst.in')
   rewind 1
   open(unit=2,file='pvst.dat')
   rewind 2
   open(unit=3,file='pvst.tpro')
   rewind 3
```

```
      read(1,*)ci,cf,npnts
      read(1,*)width,rsheet,tnot,tsubstrate,length,ns
      read(1,*)ucon
c     tnot stands for the ohmic contact temperature
c     tsubstrate stands for the phonon temperature
c     ucon stands for the prefactor in Price's equation

      curent = ci
c     step = sqrt((cf*cf-ci*ci)/float(npnts-1))
      step = (cf-ci)/float(npnts-1)
      lorentz = 2.440E-8
c     start the current loop
      do 1 icurent = 1,npnts
      ACONST = - lorentz / ( 2.0 * rsheet * ns)
      BCONST = ucon / (sqrt(ns)* ns)
      CCONST = BCONST*(tsubstrate ** 5)
      & +((curent/width)**2)*(rsheet/ns)

c     WRITE(6,*) ACONST,BCONST,CCONST
        itmax = 10000
      time =0.0
      x(1) = 0.0
      dx = length / imax
c*************************************************************

        do 10 i=2,imax
```

```
        x(i)=x(i-1)+dx
10    continue

      do 20  i=1,imax
      t(i)=tnot
      sq(i)=t(i) * t(i)
20    continue

do 1000 iter =1,itmax

   dt = 0.85 * 0.5  * dx * dx / ACONST
   if (BCONST .ne. 0.0) then
      do 30 i=1,imax
         dt2 = BCONST * 2.5 * (tsq(i)**1.5)
         dt2 = 1.0 /dt2
         if (dt2 .gt. 0.0)  dt =amin1(dt,dt2)
30    continue
   endif
      do 35 i=1,imax
         dt3 = tsq(i) / abs(CCONST)
      dt = amin1(dt,dt3)
35    continue

   time =time+dt
   do 40 i=2,imax-1
      d2tdx2 = (tsq(i+1)-2.0*tsq(i)+tsq(i-1))/(1.0*dx*dx)
      TERM1 = ACONST * d2tdx2
```

```
      TERM2 = - CCONST
      TERM3 = BCONST * (tsq(i)**2.5)
      tsq(i) = tsq(i) + dt * ( TERM1 + TERM2 + TERM3)
         if(Tsq(i).lt.0)then
         Write(6,*)'stop:ERROR',curent,tsq(i)
         Write(6,*)'sqr(t) is negative'
         Stop
         endif
      t(i) =sqrt(tsq(i))
40    continue
1000     continue

   write(2,*)t((imax+1)/2),(rsheet)*(curent**2)*(length/width)
   do 50 i=1,imax
   write(3,*)i,x(i),t(i),(rsheet)*(curent**2)*(length/width)
50    continue

   curent = curent + step
1  continue
   stop
   end
```

Appendix B

Fabrication Notes

General:

A small wafer piece, roughly 4.5 mm by 4.5 mm, was used to conserve the limited amount of heterostructure available, and to fit into the 24 pin header used in the cryostat. With such small chips, photoresist (PR) beads at the edges and corners were a major problem. We designed a perimeter clean mask that covered the entire chip except its edges in order to remove the PR beads by exposing and developing them. At times, the beads were so thick that more than one exposure was needed and by the time the perimeter was clean the center of the sample had spent so much time in the developer that its performance suffered. This was resolved by simply scraping the beads off the corners of the sample with a razor blade immediately after spinning on the PR, moving the blade inside out to prevent pile up of PR.

Shipley 1470 PR was used for the etch steps and Hoechst AZ 5218E was used in an image reversal process for lift off steps. The patterns were exposed using a HTG mask aligner. The small chips could not always be pressed flat against the mask plate even when the chuck float was used. This problem was solved by placing a clean 2-inch Si wafer on the chuck, pressing it against the mask, floating the chuck so it was parallel to the mask, and then releasing the float to fix the chuck. The sample was then placed on the chuck and brought into contact with the chuck float off. This greatly improved the uniformity of contact over the chip. All photoresist developing steps were done with Shipley Microposit 351, 1:5 in DI water, T ≈ 21 C. All baking was done on a hotplate. Note that the center of the hot plate is hotter than the corners by as much as few degree Celsius.

Standard cleaning procedure:

Rinse in flowing deionized water (DI) for 60 s or more.

Clean in trichloroethane, acetone and methanol each for 5 s with ultrasonic agitation and t 60 s plain soaking.

Blow dry with N_2 (No DI).

Bake at T > 100 C for about 3 minutes to dehydrate.

Black spots of sizes up to tens of μm that are not removed by ultrasonic cleaning are probably pits in surface from MBE growth. They cannot be removed. They will grow slightly during the mesa etch step.

Ohmic Contacts:

Clean and dry the chip. Glue to glass slide (#2 thickness is best) with PR, bake at 90 C for 2 minutes. Spin cool for 40 s at 6000 rpm.

Spin AZ5218 PR at 6000 rpm, 40 s. Scrape edges with blade to remove PR beads.

Softbake at 90 C for 5 minutes.

Expose perimeter clean pattern with a dose of ≈ 450 mJ/cm^2 at 365 nm.

Develop pattern for 23 s.

Expose pattern with ≈ 35 mJ/cm^2 at 365 nm. (Lower dose gives more undercut but rounds corners and makes holes bigger than design size. If contact is not good over pattern region because chuck is not parallel to mask or perimeter is not clean, dose will need to be increased slightly.)

Bake at 115 C for 100 s.

Flood expose with a dose of ≈ 450 mJ/cm^2.

Develop for 23-26 s.

Examine: Undercut should be visible as a faint but distinct double line around all cleared areas.

Clean PR pieces by O_2 plasma (1 kV, 1 mA, 5 minutes, P ≈ 200 mTorr)

Bake at 130 C for 10 minutes. (Lower temperature bake risks cracking during evaporation.)

Examine: Should look the same as before plasma, or maybe slightly darker at edges of cleared areas.

Strip oxide in 3% NH_4OH in H_2O with 1 drop of FL-70 detergent for 50 ml of solution by soaking for 10 s. No DI rinse. Blow and spin dry, then immediately place in evaporator and pump down.

Evaporate 350 Å of Ni, 500-550 Å of Ge and 2000-2300 Å of Au in that order using the Varian thermal evaporator.

Lift off in acetone. If PR does not come off easily let it sit for hours if necessary. If it still doesn't come off, try brief ultrasonic and/or squirting acetone with a fine needle. Do not take the sample out of the acetone, because the slightly peeled metal might fall back onto the sample and stick forever.

Measure the metal thickness on the cover slip using the Dektak. This allows confirming the accuracy of the crystal monitor of the Varian evaporator.

Rapid thermal anneal at 425 C for 60 s in flowing N_2.

Examine: Contacts should be dull yellow, not bright yellow like just after evaporation. Any bubbles in contacts should be small and uniformly distributed.

The cap layer of Au (≈ 750 Å) can be deposited using the procedure for gate metal deposition.

Mesa Etch:

Clean and dry. Glue to glass slide (#2 thickness is best) with PR, bake at 90 C for 2 minutes. Spin cool at 6000 rpm for 40 s.

Spin Shipley 1470 PR at 6000 rpm for 40 s.

Scrape PR beads from corners of sample.

Softbake at 90 C for 5 minutes.

Expose perimeter clean pattern with ≈ 450 mJ/cm^2 at 365 nm.

Develop pattern for 11 s.

Expose pattern with ≈ 115 mJ/cm^2 at 365 nm.

Develop pattern for 60–90 s.

Optional: O_2 plasma clean (1 kV, 1 mA, 5 minutes.).

Bake at 110 C for 10 minutes.

Mix etch solution: 5 ml of 30% NH_4OH, 1 ml of 30% H_2O_2, 5 drops of Fischer FL-70 detergent in 1000 ml of H_2O. It is very essential to use fresh chemicals in this step.

Wait until etch reaches T ≈ 21 C. Hold sample with locking forceps and stir gently while etching. Etch rate depends on layer structure of wafer. For the wafers used, it was close to 4-5 Å/s. Measure electrical isolation at the probe station (an isolation in dark at room temperature of the order of 10 MΩ is more than sufficient). If necessary, repeat etch procedure.

Strip PR in acetone.

Measure etch depth with Dektak.

Gate metal :

Same photolithography as for ohmic contacts.

Examine after developing: undercut should be visible as a distinct double line around all cleared areas. The alignment marks should be separated by PR of almost unchanged color; corners should not be too rounded.

Follow the same O_2 plasma, hard bake and oxide strip steps as for ohmic contacts.

Evaporate 50 Å of Ti (using a Ti rod) and enough Au to cover the depth of the mesa plus ohmic metal.

Lift off in acetone.

Other steps

Dicing a wafer:

Spin and bake a thick coat of PR on front of wafer to avoid scratches or damage to surface.

Mark back side of wafer with pencil.

Scribe lightly along pencil marks using a clean edge as a guide (e.g. a plastic ruler).

Break over the clean edge.

Rinse in DI to remove particles. Use 5s ultrasonic agitation to get rid of all particles.

Strip PR in acetone.

Cleaning Masks:

Blow off loose chunks of PR with full pressure nitrogen nozzle next to HTG mask aligner.

Soak in acetone to remove PR. Use 5-10s seconds of ultrasonic agitation if necessary.

Wash thoroughly with DI, blow dry immediately. If there is spotting from droplets of DI, squirt with isopropanol after DI wash and then immediately blow dry.

Optical Masks

The chrome on quartz optical masks were used because the pattern is less susceptible to wear and tear with repeated usage as compared to glass emulsion masks. With assistance from Gary Bordanaro and Mike Rooks, these were easily made using the optical pattern generator at the National Nanofabrication Fescility (NNF), Cornell. More effort went into creating the design using L-Edit and having it read properly by the NNF CAD system.

This appendix was based on the thesis by Keller, 1995.

Appendix C

Weak Localization

C.1) Weak Localization Fit Program

The 2D WL theory [Hikami, 1980] predicts

$$\frac{\delta R}{R}=\frac{e^2\rho}{\pi h}\left[-\frac{3}{2}\psi\left(\frac{1}{2}+\frac{H_\phi+\frac{4}{3}H_{SO}}{H}\right)+\frac{1}{2}\psi\left(\frac{1}{2}+\frac{H_\phi}{H}\right)+\frac{1}{2}\psi\left(\frac{1}{2}+\frac{H_{tr}}{H}\right)+\frac{1}{2}\ln\left(\frac{\left\{H_\phi+\frac{4}{3}H_{SO}\right\}^3}{H_\phi {H_{tr}}^2}\right)\right]$$

where Ψ is the digamma function,

$$\frac{\delta R}{R}\equiv\frac{\Delta R(T,H)-\Delta R(T,H=0)}{R(T,H=0)}$$

and

$$H_\alpha=\frac{hc}{8\pi e {L_\alpha}^2},$$

where α represents the scattering mechanism.

The following program (written for the software Igor) gives the routine to extract the phase coherence length, L_ϕ, based on the above equation. The input parameters in the fit are the spin orbit scattering length, L_{SO}, sheet resistance, electron mean free path, l, and L_ϕ. For low density samples where $L_{SO} > L_\phi$, the fit was found to be insensitive to the value of L_{SO} as long as it was larger than its theoretically [from Dresselhaus *et al.*, 1992,

we find L_{SO} to be 13 μm for sample A] predicted value. For high density samples, where $L_{SO} < L_{\phi}$, the fit gave a constant value of L_{SO}. This is consistent because SO scattering is independent of electron temperature at liquid Helium temperatures. The sheet resistance and the mean free path are experimentally determined input parameters. The fit is made to the field range $H < 0.5\ H_{tr}$, over which the theory is known to be accurate. Thus we can determine L_{ϕ}, the only other parameter in the fit.

Function/D WL_2D(W, H)

```
Wave/D W        | W[0] is Lφ, W[1] is LSO (in microns), W[2] is ρ, W[3] is l (in microns)
Variable/D H    | H is magnetic field (in Gauss)
Variable/D  Phi_not = 41.36    | Flux quantum in Gauss-sq. microns
Variable/D    L2
Variable/D    Xphi    | H/Hφ
Variable/D    X2      | H/H2
Variable/D    Y1
Variable/D    Y2
Variable/D    Y3
Variable/D    Y4
Variable/D    X3      | H/Htr
if  (H == 0)  then
    return  0
   else
        L2 = sqrt(1/ (1/(W[0]*W[0]) + 4/(3*W[1]*W[1]) ) )
        Xphi =8*pi*W[0]*W[0]*abs(H)/Phi_not
        X2 =8*pi*L2*L2*abs(H)/Phi_not
```

```
        X3 =4*pi*W[3]*W[3]*abs(H)/Phi_not
        Y1 = DiGamma(0.5 + 1/Xphi)
        Y2 = DiGamma(0.5 +1/ X2)
        Y3=  DiGamma(0.5 +1/ X3)
        Y4=((W[0]*W[0]*W[3]*W[3]*W[3]*W[3])/(L2*L2*L2*L2*L2*L2))*0.25
    return  1.23e-5 * W[2] * (-1.5*Y2 + 0.5*Y1 + Y3 + 0.5*ln(Y4) )
  endif
End
```

Function/D DiGamma(x)

```
  Variable/D  x
  Variable/D cutoff = 200
  Variable/D    NumTerms = 200        | Number of terms to sum using exact form
  Variable/D    Sum
  Variable/D  i
  if (x> cutoff) then
    return     ln(x) - 1/(2*x) - 1/(12*x*x) + 1/(120*x*x*x*x)
  else
    Sum = ln(x)
    i = 0
    do
      Sum += ln(1 + 1/(x+i)) - 1/(x+i)
      i += 1
    while(i <= NumTerms)
  return  Sum
  endif
```

End

C.2) Phase Coherence Length in GaAs 2DEGs Below 0.5K

The dominant phase breaking mechanism in GaAs 2DEGs below 0.5K is believed to be due to electron-electron scattering in the presence of impurities. The phase breaking rate due to this mechanism, known as the so-called Nyquist rate, is predicted [Altshuler, 1982] to be

$$\tau_\phi^{-1} = \left(\frac{k_B}{2 E_F \tau_{tr}} \ln \frac{E_F \tau}{\mathrm{h}} \right) T .$$

Although the temperature dependence $\tau_\phi^{-1} \propto T$ has been confirmed [see review by Beenakker *et al.*, 1991], the accuracy of the prefactor is not well established. Nonetheless, using the above expression, we can estimate the phase coherence length as $L_\phi = \sqrt{(D\tau_\phi)}$, where D is the diffusivity. For sample A, this gives $L_\phi^{-2} = 0.07$ T. As a comparison, the linear fit to the experimental data for Sample A (Figure 5.2) gives us $L_\phi^{-2} = 0.16$ T. Thus we are confident that not only are we seeing the right temperature dependence (which is the requisite for using the phase coherence length's temperature dependence as a thermometer for the electron gas), but also the correct magnitude.

Appendix D

Sample Mount in the Dilution Refrigerator

The details of the mixing chamber and sample mount* in the dilution refrigerator are shown in Figure D.1. The mixing chamber itself was made out of copper and was attatched to a copper plate with several threaded bolts. An extension rod of copper and epoxy, desgined by Oxford to minimize eddy current heating, was screwed into the bottom of the mixing chamber plate. The lower end of that extension had brass threads and a flat copper stub at the center. The copper post that supported the sample mount was held tightly against that stub by a brass nut, both copper faces having been polished and cleaned for good thermal conductance. This ensured that the copper post was at the mixing chamber temperature for all practical heat loads. The copper post was soldered to a Y shaped copper piece. Each arm of the Y supported a circular piece of G-10 epoxy which held the sockets. The G-10 piece contained sockets matched to headers with 8, 16, and 24 pins to accommodate the samples of various groups who used the dilution refrigerator.

The wiring for the sample mount was as follows. Copper leads, 30 AWG. with polythermaleze insulation, were wrapped several times on coper post screwed into the mixing chamber plate. Below that they were wrapped tightly around the copper post just above the sample mount and held in place with GE 7031 varnish. The 24 sample leads were split just above the G-10 piece so that each one was connected to one socket for the 24 pin headers and one socket for the 8 or 16 pin headers. This allowed samples on 8 and 16 pin headers to be cooled and measured simultaneously. Samples on 16 and 24 pin headers could be used together as long as not all of the pins on each header were required. Each lead was attached with a combination of SnPb solder joints and removable

* Sample A was measured in an earlier sample mount (for details, see Keller, 1995). The wiring for this sample mount was essentially identical with the one described here.

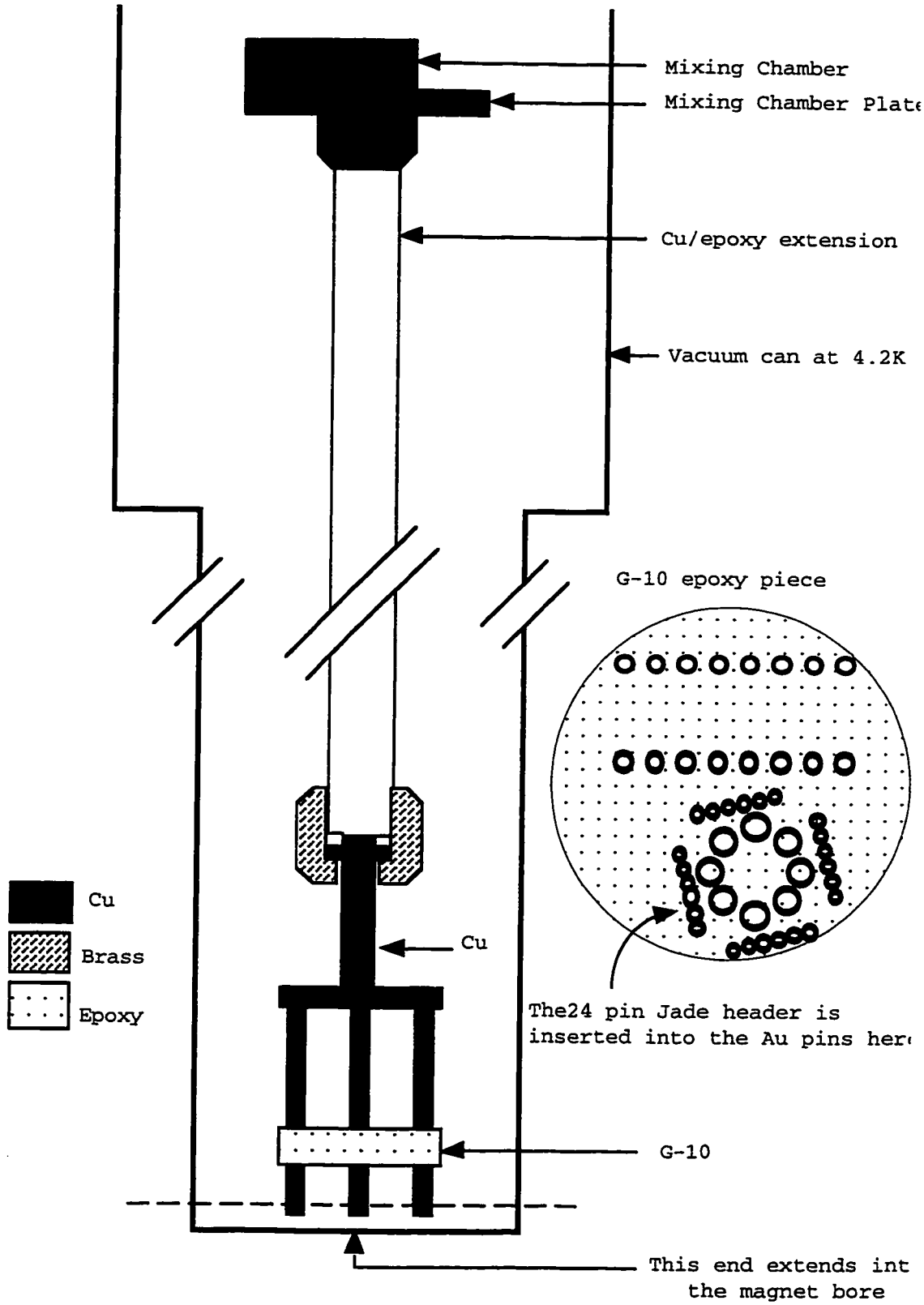

Figure D.1 Mixing chamber and sample mount (wiring not shown).

mechanical contacts such that the assignment of leads to sockets could easily be changed. One or two RuO sensors were attached to leads wrapped in the same way. The sensors were then placed in holes drilled in the Cu post or taped to one of the arms of the "Y" with Cu tape.

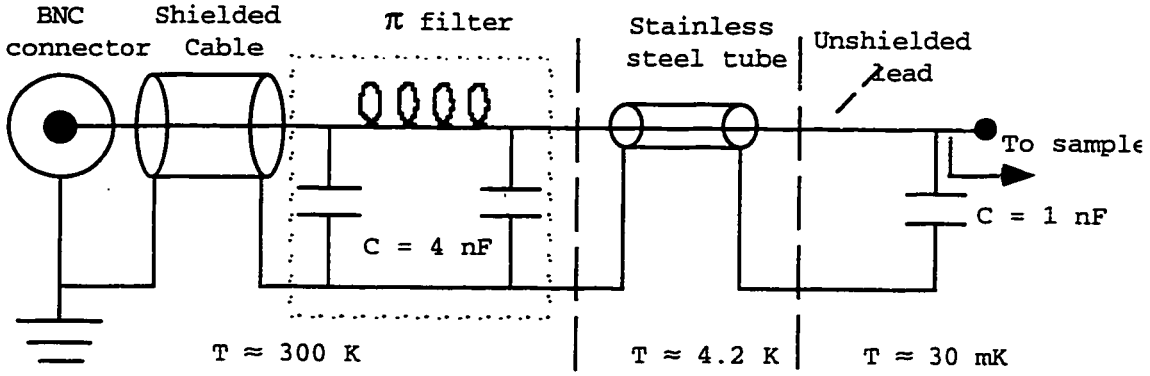

Figure D.2. Schematic picture showing shielding and filtering of a sample lead.

The shielding and filtering used for the sample leads is shown in Figure D.2. All cable connections for the four probe resistance measurements entered the cryostat in shielded cable with D-25 connectors so that commercial pi filters could be inserted into the signal line outside the cryostat. Inside the metal cryostat the leads passed through the liquid He bath inside a stainless steel tube and entered the vacuum can. Inside the vacuum can the leads were not shielded. Between the mixing chamber and the sample mount a polyester film capacitor (C = 1 nF) was soldered to each lead to create a low impedance path for the high frequency noise to the mixing chamber, which was at the same potential as the vacuum can and the stainless steel tube. The leads for the RuO thermometers were filtered in the same way. This appendix was based on the thesis by Keller, 1995.

Bibliography

Altshuler, B.L., Aronov, A.G., and Khmelnitsky, D.E. (1982), *J. Phys. C: Solid State Phys.*, **15**, 7367.

Altshuler, B.L., Aronov, A.G., Khmelnitsky, D.E., and Larkin, A. I. (1982) in *Quantum Theory of Solids*, edited by Lifshitz, I. M. (MIR Publishers, Moscow).

Ashcroft, N. W., and Mermin, N. D. (1988), *Solid State Physics*, Saunders College, Philadelphia.

Beenakker, C.W.J., and van Houten, H. (1991), in *Solid State Physics*, Vol. 44, edited by Ehrenreich, H., and Turnbull, D. (Academic Press, New York).

Belitz, D., and Das Sarma, S. (1987), *Phys. Rev.* **B36**, 7701.

Bergmann, G. (1984) *Physics Reports* **107**, 1.

Bergmann, G., Wei, W., Zhou, Y., and Mueller, R.M. (1990), *Phys .Rev.* **B41**, 7386.

Blyumina, M.G., Denisov, A.G., Polyanskaya, T.A., Savel'ev, I.G., Senichkin, A.P., and Shmartsev,Yu.V. (1986), *Pis'ma ZhETF* **44**, 257.

Braslau, N. (1981), *J. Vac. Sci. Technol.* **19**, 803.

Challis, L.J. (1993), in *The Physics of Low-Dimensional Semiconductor Structures*, edited by Butcher *et al.*, Plenum Press, New York.

Chow, E., WEi, H.P., and Girvin, S. M. (1996) submitted to *Phys. Rev. Lett.*

DiTiusa, J.F., Lin, K., Park, M., Issacson, M.S., and Parpia, J.M. (1992), *Phys. Rev. Lett.* **68**, 1156.

Dresselhaus, P. D., Papavassiliou, C. M. A., and Wheeler, R. G. (1992), *Phys. Rev. Lett.* **68**, 106.

Dresselhaus, P.D. (1992), Ph.D. Thesis, Yale University.

Gantmakher, V.F., and Levinson, Y.B. (1987), *Carrier Scattering in Metals and Semiconductors*, Elsevier Science Publishers, Netherlands.

Gershenson, E.M., Gershenson, M.E, Gol'tsnman, G.N., Lyu'kin, A.M.,Semenov, A.D., and Segeyev, A.V. (1990), *Sov. Phys. JETP* **70**, 505.

Hikami, S., Larkin, A.I., and Nagaoka, Y. (1980) *Prog. Theor. Phys.* **63**, 707.

Hirakawa, K., and Sakaki, H. (1986) *Appl. Phys. Lett.* **49**, 9744.

Ismail, K., Washburn, S., and Lee, K.Y. (1991), *Appl. Phys. Lett.* **59**, 1998.

Karpus, V. (1988), *Sov. Phys. Semicond.* **22**, 268.

Keller, M.W. (1995), Ph.D. Thesis, Yale University.

Klepper, S.J. (1991), Ph.D. Thesis, Yale University.

Kreschuk, A.M., Martisov, M.Yu., Polyanskaya, T.A., Savel'ev, I.G., Saidashev, I.I., Shik, A.Ya.,and Shmartsev, Yu.V. (1988),*Solid State Commun.* **65**, 1189.

Lee, K.Y., Kern, D.P., Ismail, K., and Washburn, S. (1991), *J. Vac. Sci. Technol.* **B9**, 2834.

Lifshitz, I.M. (1952) *Sh. Ekdsp. Teir. Fiz.* **22**, 475.

Manion, S. J., Artaki, M., Emanuel, M. A., Coleman, J. J., and Hess, K. (1987), *Phys. Rev.* **B35**, 9203.

Lounasmaa, O.V. (1988), *Experimental Principles and Methods Below 1K*, Academic Press, San Diego.

Ma, Y., Fletcher, R., Zaremba, E., D'Iorio, M., Foxon, C.T., and Harris, J.J. (1991) *Phys. Rev.* **B43**, 9033.

Price, P.J. (1981),*J. Vac. Sci. Technol.* **19**, 599.

Price, P.J. (1982),*J. Appl. Phys.* **53**, 6863.

Prober, D.E. (1993), *Appl. Phys. Lett.* **62**, 2119.

Ptitsina, N.G., Chulkova, G.M., Gershenson, E.M., and Gershenson, M.E. (1995), *Sov. Phys. JETP* **80**, 960.

Rammer, J., and Schmid, A. (1973), *Phys. Rev.* **B34**, 1352.

Reizer, M.Y., and Sergeyev, A.V. (1986), *Sov. Phys. JETP* **63**, 616.

Richter, C.A. (1993), Ph.D. Thesis, Yale University.

Ridley, B.K. (1991), *Rept. Prog. Phys.* **54**, 169.

Robinson, G.Y. (1975), *Solid State Electronics* **18**, 331.

Santhanam, P., Wind, S., and Prober, D.E. (1987) *Phys. Rev.* **B35**, 3188.

Stern, F. (1967), *Phys. Rev. Lett.* **18**, 546.

Takayama, H. (1973), *Z. Phys.* **259**, 421.

Verevkin, A.A., Ptitsina, N.G., Chulcova, G.M., Gol'tsman, G.N., Gershenson, E.M., and Yngvesson, K.S. (1996), *JETP Lett.*, **61**, 591.

Vion, D., Orfila, P.F., Joyez, P., Esteve, D., and Devoret, M.H. (1996) to appear in *J. Appl. Phys.*

Wennberg, A.K.M., Ytterboe. S.N., Gould, C.M., Bozler, H.M., Klem, J., and Morkoc, H., (1986) *Phys. Rev.* **B34**, 4409.

Ziman, J.M. (1979), *Principles Of The Theory Of Solids* , Cambridge University Press.